RESONANT CYCLOTRON SCATTERING IN THREE DIMENSIONS AND THE QUIESCENT NONTHERMAL X-RAY EMISSION OF MAGNETARS

Rodrigo Fernández[1] and Christopher Thompson[2]

ABSTRACT

Although the surface of a magnetar is a source of bright thermal X-rays, its spectrum contains substantial nonthermal components. The X-ray emission is pulsed, with pulsed fractions that can be as high as ~70%. Several properties of magnetars indicate the presence of persistent, static currents flowing across the stellar surface and closing within the magnetosphere. The charges supporting these currents supply a significant optical depth to resonant cyclotron scattering in the 1–100 keV band. Here we describe a Monte Carlo approach to calculating the redistribution of thermal seed photons in frequency and angle by multiple resonant scattering in the magnetosphere. The calculation includes the full angular dependence of the cyclotron scattering cross section and the relativistic Doppler effect due to the motion of the charges and allows for an arbitrary particle velocity distribution and magnetic field geometry. We construct synthetic spectra and pulse profiles for arbitrary orientations of the spin axis, magnetic axis, and line of sight, using a self-similar, twisted dipole field geometry and assuming that the seed photons are supplied by single-temperature blackbody emission from the stellar surface. Pulse profiles and 1–10 keV spectra typical of anomalous X-ray pulsars (AXPs) are easily produced by this model, with pulsed fractions of ~50%. However, this model cannot reproduce the hard, rising energy spectra that are observed from soft gamma repeaters (SGRs) during periods of activity without overproducing the thermal emission peak. This suggests that the 1–100 keV emission of SGRs has a common origin with the hard X-ray emission detected from some AXPs above ~20 keV.

Subject headings: plasmas — radiative transfer — scattering — stars: magnetic fields — stars: neutron — X-rays: stars

1. INTRODUCTION

Magnetars have many remarkable properties that appear to derive from the decay of an ultrastrong magnetic field. Measurements of spin-down torques and bright X-ray outbursts have revealed dipole fields as strong as ~10^{15} G and imply the existence of internal fields an order of magnitude stronger in some objects (Thompson & Duncan 1996; Woods & Thompson 2006). More recent measurements strongly suggest that the external magnetic field can support electric currents that are several orders of magnitude larger than the Goldreich-Julian current that flows along the open field lines. In some magnetars, the injection of these closed-field currents into the magnetosphere appears to be associated with soft gamma repeater (SGR) burst activity; but in others, the current appears to be sustained in the absence of bright SGR outbursts, namely, in the class of magnetars known as the anomalous X-ray pulsars (AXPs).

The basic properties of a twisted neutron star magnetosphere were outlined by Thompson et al. (2002). A detailed one-dimensional plasma model of the current in the closed magnetosphere has been constructed by Beloborodov & Thompson (2007). The presence of such a global twist has several observational effects, which mirror the behavior of magnetars in the following ways.

Correlation between spin-down torque and X-ray hardness.— The presence of a twist in the external magnetic field causes it to flare out slightly. As a consequence, the open-field flux is larger than that estimated from the dipole model, and the spin-down torque is increased. The charges flowing along the twisted closed field lines also supply a significant optical depth to resonant cyclotron scattering. This optical depth is independent of radius (resonant frequency) when the magnetosphere is self-similar. The thermal photons emitted from the surface of the star are multiply scattered. Thus, the observed correlation between the spin-down torque and the hardness of the power-law component of the 1–10 keV X-ray spectrum (Marsden & White 2001) can be explained by adjusting a single parameter: the angle through which the magnetospheric field lines are twisted (Thompson et al. 2002).

Persistent changes in X-ray pulse profiles.—Following the 1998 giant flare, the pulse profile of SGR 1900+14 changed to a single, nearly sinusoidal peak from a more complicated profile with multiple peaks that was observed before the flare (Woods et al. 2001). The change in the pulse profile persisted even though the quiescent X-ray flux returned to its preburst level. Something similar happened to SGR 1806−20 after its 2004 giant flare, except that instead of simplifying, the pulse profile became more complex (Woods et al. 2007). The AXP 1E 2259+586 also showed a systematic change in pulse profile following the 2002 outburst, although the duration of the change was shorter lived than in the SGRs (Woods et al. 2004). It appears that the external magnetic field of a magnetar is reconfigured following a period of burst activity (Woods et al. 2001; Thompson et al. 2002).

Persistent changes in $\dot{P}$.—The spin-down torque of SGR 1900+14 and SGR 1806−20 can show large-amplitude modulations, increasing over the previous long-term trend by at least a factor of ~4 (Woods et al. 2007, and references therein). The increase sets in gradually several months after a period of burst activity and then persists for years. Related but less dramatic effects are seen in the torque behavior of some AXPs (Gavriil & Kaspi 2004).

Hard X-ray emission.—Emission above 20 keV has been measured from both SGRs and AXPs (Kuiper et al. 2004, 2006; Götz

[1] Department of Astronomy and Astrophysics, University of Toronto, Toronto, ON M5S 3H4, Canada.
[2] Canadian Institute for Theoretical Astrophysics, Toronto, ON M5S 3H8, Canada.

et al. 2006, and references therein). The SGRs in their most active states show a hard, rising energy spectrum between 1 and 100 keV. In the AXPs, the spectrum often shows a strong upward break between 10 and 50 keV. In both classes of sources, the output at 100 keV can be 10 times stronger than the thermal emission from the neutron star surface. It appears that the bolometric output of these objects is dominated by the magnetosphere. The additional high-energy component could be explained by bremsstrahlung emission from the transition layer near the neutron star surface or possibly by a pair cascade at $\sim$100 km from the neutron star (Thompson & Beloborodov 2005).

In this paper we confront the magnetar model with some of the observational evidence listed above. We focus on the part of the nonthermal X-ray spectrum that lies directly above the blackbody peak and also on the X-ray pulse behavior in this band (the first and second items above). The most robust way of testing the twisted magnetosphere hypothesis is to produce synthetic analogs of observable quantities, using the self-similar model developed by Thompson et al. (2002). The radiation transport through the magnetosphere is sensitive to several geometrical effects, which include the angular emission pattern of cyclotron scattering by moving charges, the magnetic field geometry, the orientation with respect to the observer, and the particle velocity distribution.

A first strategy is to ignore all the geometrical complications, focusing on the essential physics entering the multiple scattering process in a one-dimensional geometry. The problem of radiation transport through the accretion column of an X-ray pulsar has been treated in this way, using both Feautrier's method to solve the radiation transport equation (Mészáros & Nagel 1985a, 1985b) and Monte Carlo techniques (Pravdo & Bussard 1981; Wang et al. 1988). The more general problem of the transfer of X-ray photons through a single resonant surface has been analyzed by Zheleznyakov (1996) and Lyutikov & Gavriil (2006) by restricting the transfer of photons to one spatial dimension and assuming a subrelativistic and thermal distribution of scattering charges.

We do not expect narrow spectral features to form as a result of the transfer of thermal X-ray photons through the quiescent, twisted magnetosphere. The cyclotron optical depth is regulated to a value close to unity over a broad range of frequencies. By contrast, the optical depth is much higher in a pulsar accretion column and is concentrated over a narrower range of radius and magnetic field. (In addition, the equivalent width of the absorption feature that forms in the cold atmosphere of a passively cooling magnetar is suppressed by polarization mode exchange [Ho & Lai 2004].) The optical depth varies significantly with angle in the twisted dipole magnetic field, and the field lines impart a nontrivial angular structure to the particle velocity distribution. This means that a numerical simulation in three dimensions is required to model the formation of a high-energy tail in the spectrum and the amplitude and shape of the X-ray pulses that are seen by a distant observer.

In this paper we report the development of a Monte Carlo code that follows the transfer of X-ray photons through the stellar magnetosphere, with resonant cyclotron scattering as the source of opacity. The code treats the scattering problem in three dimensions for an arbitrary magnetic field geometry and an arbitrary velocity distribution of the scattering charges. We account for the relativistic Doppler effect and polarization exchange during scattering, but neglect the effects of recoil (which are important only at high energies where the spectra of AXPs and SGRs are not well measured and where additional emission components are sometimes observed). The output spectra and pulse profiles are obtained for an arbitrary line of sight and for an arbitrary orientation of the spin axis and magnetic axis of the neutron star.

The paper is structured as follows. In § 2 we review the physical input to the model, and in § 3 we describe the Monte Carlo code. Results are presented and discussed in detail in § 4. A comparison with the existing data and general conclusions follow in § 5.

2. RESONANT CYCLOTRON SCATTERING IN A NONPOTENTIAL MAGNETOSPHERE

In this section we describe the physical model that we are simulating. We first review the properties of a neutron star magnetosphere that carries a net twist (Thompson et al. 2002). We then review the process of resonant cyclotron scattering and how it depends on the structure of the magnetosphere. At frequencies lower than the surface cyclotron frequency, the optical depth depends only on the twist angle and the drift speed of the charges. The effects of relativistic particle motion are considered in detail.

In the magnetar model, there are two sources of keV photons. The first is deep cooling. As the internal magnetic field is transported outward, part of the field energy is converted to heat, and the remainder to a deformation of the magnetic field outside the star. Part of this internal heat is conducted to the surface, and the remainder is radiated as neutrinos (Thompson & Duncan 1996). This component of the blackbody flux will be carried by the E-mode, given that its opacity is strongly suppressed in the surface layers by a factor $\sim (m_e c \omega / eB)^2 \sim 0.1 (k_B T_{bb} / m_e c^2)^2 B_{15}^{-2}$ (Silantev & Iakovlev 1980).

The impact of current-carrying particles on the surface is a second possible source of kilo–electron volt photons (Thompson et al. 2002). Some fraction of the particle kinetic energy will be deposited in a layer that is optically thick to the O-mode, but optically thin to the E-mode. This energy would then be reradiated in the O-mode with a nearly blackbody frequency distribution. Although ions are probably able to penetrate this deep, it has been argued that a relativistic electron (or positron) beam will deposit a significant fraction of its energy in an optically thin layer, which is reemitted in the O-mode at a much higher temperature (Thompson & Beloborodov 2005).

A recent recalibration of the distance to several AXPs shows that their 1–10 keV luminosities are tightly clustered around $\sim 1 \times 10^{35}$ ergs s^{-1} (Durant & van Kerkwijk 2006a). These sources have a range of spin-down rates, and their X-ray spectra are of variable hardness. The clustering of the 1–10 keV emission therefore suggests that the rate of heat conduction to the surface is buffered by bulk neutrino cooling, and that the blackbody emission is not dominated by particle heating. However, in the active SGRs and at least one AXP, the magnetospheric output at $\sim$100 keV is significantly brighter than the $\sim$1 keV surface emission (Kuiper et al. 2004, 2006; Götz et al. 2006) and is more comparable to the expected neutrino luminosity (Thompson & Duncan 1996). This suggests that a significant fraction of the energy that is released by the untwisting of the internal magnetic field ends up in a quasistatic deformation of the external magnetic field, such as we are assuming in this paper.

A photon propagating away from the surface of a magnetar can scatter resonantly at a significant rate over some part of its path. If the magnetospheric particles had a narrow velocity distribution of width $\Delta \beta c$, then the cyclotron scattering would be localized on a "resonant surface" with a well-defined radius R_{res} and a thickness $\Delta R_{res} \sim \Delta \beta R_{res}$. A similar statement holds for any photon after it has been resonantly scattered within the magnetosphere.

The transfer of thermal photons through a single warm scattering layer (with one-dimensional electron temperature $k_B T_\parallel \ll m_e c^2$)

results in a second component of the spectrum that is upshifted in frequency by a factor $1 + 2(k_B T_\parallel/m_e c^2)^{1/2}$ (Lyutikov & Gavriil 2006). This analytic result is, however, restricted to one spatial dimension, does not include the bulk motion of the charges, neglects the effect of scattering at distant points in the magnetosphere, and becomes inaccurate when the r.m.s. speed of the charges exceeds[3] $\beta \simeq 0.3$.

In a more realistic, three-dimensional magnetosphere, a power-law component of the spectrum results from two effects:

1. Multiple resonant scattering within a single magnetic hemisphere, in which the charge flow is converging and the average increase $\Delta\omega$ in photon frequency per scattering is first order in β;

2. Multiple scatterings in different magnetic hemispheres, for which $\Delta\omega \sim \beta^2$ if the projection of the particle drift speed onto the magnetic axis is the same in the two hemispheres.

For example, when the charge flow in the twisted magnetosphere is carried by electrons and positrons, each hemisphere will contain one species of charge whose bulk motion is directed toward the star. Even when electrons are the only species of light charge (the positive charge flow being carried by ions), the electron velocity will converge in one magnetic hemisphere. The optical depth is independent of frequency in a self-similar magnetosphere, and a significant fraction of the backscattered photons undergo multiple scatterings if the field is twisted through $\sim$1 radian (Thompson et al. 2002; eq. [11]).

2.1. Twisted Self-Similar Magnetospheres

Thompson et al. (2002) solved the force-free equation $\boldsymbol{J} \times \boldsymbol{B} = 0$ outside a spherical surface with a self-similar *Ansatz* (Lynden-Bell & Boily 1994; Wolfson 1995). These solutions form a one-parameter sequence, labeled by the net twist angle of the field lines that are anchored close to the magnetic poles,

$$\Delta\phi_{\text{N-S}} = 2 \lim_{\theta_0 \to 0} \int_{\theta_0}^{\pi/2} \frac{B_\phi(\theta)}{B_\theta(\theta)} \frac{d\theta}{\sin\theta}, \tag{1}$$

where θ and ϕ denote the polar and azimuthal angle relative to the magnetic axis. The magnetic field is

$$\boldsymbol{B}(r, \theta) = \frac{B_{\text{pole}}}{2} \left(\frac{R_{\text{NS}}}{r} \right)^{2+p} \boldsymbol{F}(\cos\theta), \tag{2}$$

where B_{pole} is the field strength at the magnetic poles, r is the radial coordinate, and R_{NS} the stellar radius. The components of $\boldsymbol{F}$ are expressed in terms of a function $f(\cos\theta)$, which is the solution to the ordinary differential equation

$$\sin^2\theta f'' + Cf^{1+2/p} + p(p+1)f = 0. \tag{3}$$

One finds $F_r = -f'$, $F_\theta = (p/\sin\theta)f$, and $F_\phi = [C/p(p+1)]^{1/2} f^{1/p} F_\theta$. The function $f(\cos\theta)$ satisfies the three boundary conditions $f'(0) = 0$, $f'(1) = -2$, and $f(1) = 0$. These force-free equilibria[4] smoothly interpolate between a dipole ($\Delta\phi_{\text{N-S}} = 0$, $p = 1$) and a split monopole ($\Delta\phi_{\text{N-S}} = \pi$, $p = 0$). The poloidal field lines remain close to a dipole as long as $\Delta\phi_{\text{N-S}} \lesssim 1$.

The current density induced along the twisted field lines is (Thompson et al. 2002)

$$\boldsymbol{J} = \sum_i Z_i e n_i \boldsymbol{\beta}_i c = \frac{(p+1)c}{4\pi r} \frac{B_\phi}{B_\theta} \boldsymbol{B} \simeq \frac{c\Delta\phi_{\text{N-S}}}{4\pi r} \sin^2\theta \boldsymbol{B}, \tag{4}$$

where $Z_i e$ is the electric charge of particle species i, n_i is the particle density, and $\boldsymbol{\beta}_i = \beta_i \hat{\boldsymbol{B}}$ is the particle velocity directed along $\hat{\boldsymbol{B}} = \boldsymbol{B}/B$ in units of the speed of light c.

The closed-field current in equation (4) implies a much higher flux of charged particles than can be supplied by the rotationally induced (corotation) charge density. As a result, the magnetospheric plasma contains both positive and negative charges with nearly equal densities (Beloborodov & Thompson 2007). One has $J/|\rho_{\text{GJ}}|c \sim \Delta\phi_{\text{N-S}}(\Omega R_{\text{max}}/c)^{-1}$, where $\rho_{\text{GJ}} = -\boldsymbol{\Omega} \cdot \boldsymbol{B}/2\pi c$ (Goldreich & Julian 1969), $\boldsymbol{\Omega}$ is the spin angular velocity of the star, and $R_{\text{max}} \simeq r/\sin^2\theta$ is the maximum radius of the poloidal field line that passes through the position (r, θ) in the magnetosphere. We consider both a unidirectional flow of the scattering charges at any given position in the magnetosphere and a bidirectional flow. The first case corresponds to an electron-ion plasma, and the second to a pair-dominated plasma.

2.2. Basic Properties of Resonant Cyclotron Scattering of X-ray Photons

When a plasma is threaded by a magnetic field, cyclotron absorption will occur whenever the condition

$$\omega = \omega_c \equiv \frac{|Z|eB}{mc} \tag{5}$$

is satisfied in the rest frame of a charged particle, where ω is the photon frequency and Ze and m are the particle charge and mass, respectively. Absorption by motionless charges occurs at a radius

$$R_{\text{res}}(\omega) = (10.5)^{3/(2+p)} R_{\text{NS}} \left[|Z| \left(\frac{B_{\text{pole}}}{10^{14}\,\text{G}} \right) \left(\frac{m_e}{m} \right) \right.$$
$$\left. \times \left(\frac{1\,\text{keV}}{\hbar\omega} \right) \xi(\theta, \Delta\phi_{\text{N-S}}) \right]^{1/(2+p)}. \tag{6}$$

For a 1 keV photon, this works out to $R_{\text{res}} \sim 200 B_{\text{pole},15}^{1/3}$ km for electrons and $20 B_{\text{pole},15}^{1/3}$ km for protons. The function ξ contains the angular dependence of the magnetic field strength;

$$\xi^2 = \frac{1 + 3\cos^2\theta}{4} \tag{7}$$

for a dipole, and

$$\xi^2 = \frac{1}{4}\left[(f')^2 + \left(\frac{pf}{\sin\theta} \right)^2 + \frac{pC}{p+1}\left(\frac{f^{1+1/p}}{\sin\theta} \right)^2 \right] \tag{8}$$

for the self-similar twisted magnetosphere (eq. [2]).

The time for a particle to lose a gyrational energy comparable to mc^2 by cyclotron emission is much shorter than the dynamical time R_{res}/c when the cyclotron energy is greater than $\sim 10^{-3}(m/m_e)^{4/5}$ eV. In this fast-cooling regime, the combined absorption and reemission can be treated as a scattering process, with a rest-frame cross section (e.g., Canuto et al. 1971; Mészáros 1992)

$$\sigma_{\text{res}} = 4\pi^2 \frac{|Z|e}{B} |e_{l,r}|^2 \omega_c \delta(\omega - \omega_c). \tag{9}$$

Here

$$e_{l,r} = \hat{\boldsymbol{e}} \cdot \left(\frac{\hat{\boldsymbol{x}} \pm i\hat{\boldsymbol{y}}}{\sqrt{2}}\right)^* \qquad (10)$$

is the overlap of the photon's polarization with a left or right circularly polarized mode (depending on whether the scattering charge is negative or positive), and $\hat{\boldsymbol{x}}$ and $\hat{\boldsymbol{y}}$ are unit vectors perpendicular to $\boldsymbol{B}$. Integrating through the cyclotron resonance yields a cross section that is much larger than Thomson by a factor $\sim (e^2/\hbar c)^{-1}(\hbar\omega_c/m_e c^2)^{-1} \sim 10^5$ for a keV photon. We neglect the electron recoil in our calculations and relativistic effects on the scattering cross section (e.g., Herold 1979). These effects start to be significant at photon energies $\gtrsim 50$ keV $\sim m_e c^2/10$ if the electrons are subrelativistic.

The surface magnetic field of the AXPs and SGRs is believed to exceed $B_{QED} = m_e^2 c^3/e\hbar = 4.4 \times 10^{13}$ G, where the energy of the first electron Landau level begins to exceed $\sim m_e c^2$. We are concerned here only with resonant scattering in the parts of the magnetosphere where the Landau levels of the scattering charges are nonrelativistic. The resonant absorption of a kilo–electron volt photon close to the surface of a magnetar creates a high-energy gamma ray that is converted to an electron-positron pair near the emission site (Beloborodov & Thompson 2007). The ion cyclotron energy is in the kilo–electron volt range even at the surface of a magnetar, so the effects of ion cyclotron scattering on the X-ray spectrum are concentrated much closer to the star. The formulae that follow generally apply only in this nonrelativistic regime.

The current from equation (4) supplies enough particles for resonant cyclotron scattering to become the dominant source of opacity in the keV range (Thompson et al. 2002; Lyutikov & Gavriil 2006). Integrating equation (9) through the resonance gives an optical depth

$$\tau_{res} \sim \frac{\Delta\phi_{N\text{-}S}}{|\beta|} \sin^2\theta. \qquad (11)$$

This expression does not depend on the mass or charge of the scattering particle and applies as long as the resonant energy is less than mc^2 and lies below the surface cyclotron energy. This result is a direct consequence of the self-similarity of the force-free construction. A more realistic magnetosphere has a more inhomogeneous distribution of twist, contains higher order multipoles, and is nonaxisymmetric.

The resonance condition is changed by bulk motion of the charges along the magnetic field lines and becomes

$$\omega = \omega_D \equiv \frac{\omega_c}{\gamma(1 - \beta\mu)}, \qquad (12)$$

where $\gamma = (1 - \beta^2)^{-1/2}$ is the Lorentz factor and $\mu = \hat{\boldsymbol{k}} \cdot \hat{\boldsymbol{B}} \equiv \cos\theta_{kB}$ is the direction cosine of the photon with respect to the magnetic field in the stellar frame. In this case, the resonant radius in equation (6) needs to be multiplied by a factor $[\gamma(1 - \beta\mu)]^{-1/(2+p)}$. Similarly, the cross section in the stellar frame equals equation (9) multiplied by $(1 - \beta\mu)$ (e.g., Rybicki & Lightman 1979), with ω_c replaced by ω_D and with $|e_{l,r}|^2$ evaluated in the rest frame of the charge,

$$\sigma_{res} = 4\pi^2(1 - \beta\mu)\frac{|Z|e}{B}\left|e'_{l,r}\right|^2 \omega_D \delta(\omega - \omega_D) \quad (\beta \neq 0). \qquad (13)$$

In what follows, the prime labels the particle rest frame.

The polarization modes of a photon in a magnetized plasma depend on the relative contributions of plasma and vacuum polarization to the dielectric tensor (e.g., Zheleznyakov 1996). Even in the core of a cyclotron resonance, vacuum polarization can dominate in a cold plasma with a velocity width $\Delta\beta \ll 1$ if the condition

$$\frac{\omega_P^2}{\omega^2|\Delta\beta|} \ll \frac{1}{45\pi}\frac{e^2}{\hbar c}\left(\frac{B}{B_{QED}}\right)^2 \quad (B < B_{QED}) \qquad (14)$$

is satisfied. In equation (14), $\omega_P = (4\pi e^2 n_e/m_e)^{1/2}$ is the electron plasma frequency. In this situation both electromagnetic eigenmodes are linearly polarized even at frequencies very close to ω_D. The extraordinary mode (E-mode) corresponds to $\hat{\boldsymbol{e}} = \hat{\boldsymbol{B}} \times \hat{\boldsymbol{k}}$, and the ordinary mode (O-mode) to $\hat{\boldsymbol{e}} = (\hat{\boldsymbol{B}} \times \hat{\boldsymbol{k}}) \times \hat{\boldsymbol{k}}$. This means that each polarization eigenmode will experience the same interaction with the gyromotion of a positron as it does with the gyromotion of an electron; the overlap

$$|e_{l,r}|^2_E = 1/2, \quad |e_{l,r}|^2_O = \cos^2\theta_{kB}/2 \qquad (15)$$

does not depend on the sense of circular polarization. In the case of unpolarized photons, $|e_{l,r}|^2_{unpol} = (1 + \cos^2\theta_{kB})/4$.

Mode exchange is clearly possible during resonant scattering (e.g., Zheleznyakov 1996; Wang et al. 1988). The differential cross section for scattering from mode A to mode B is $d\sigma_{AB}/d\Omega' \propto |e'_{l,r}(A)|^2 |e'_{l,r}(B)|^2$. The probability that any mode A is converted to the extraordinary mode is

$$P(A \to E) = \frac{|e'_{l,r}(E)|^2}{|e'_{l,r}(E)|^2 + |e'_{l,r}(O)|^2} = \frac{1}{1 + \cos^2\theta'_{kB}}, \qquad (16)$$

and the probability for conversion to the O-mode is $P(A \to O) = 1 - P(A \to E)$. These branching ratios depend on the angle (after scattering) between $\hat{\boldsymbol{k}}$ and $\hat{\boldsymbol{B}}$ in the charge rest frame,

$$\cos\theta'_{kB} = \mu' = \frac{\mu - \beta}{1 - \beta\mu}. \qquad (17)$$

2.3. Basic Degrees of Freedom of the Magnetospheric Model

The model is defined by:

The twist angle $\Delta\phi_{N\text{-}S}$.—This labels a one-parameter sequence of magnetic field geometries (eqs. [4] and [11]). We consider only axisymmetric field configurations in this paper. (Our numerical implementation can, in principle, handle more complicated, non-axisymmetric geometries.)

The spectral distribution of the seed photons.—We generally assume a blackbody distribution, defined by a single temperature T_{bb}. In numerical calculations, smoother spectra below the blackbody peak are obtained by injecting photons at a single frequency and then convolving the output spectrum with an input blackbody spectrum. We show in Appendix A that this procedure nicely reproduces the spectrum that is obtained by drawing photons directly from a blackbody distribution.

The polarization of the seed photons.—We calculate the output spectrum assuming that the seed photons are 100% polarized (E-mode or O-mode). The spectrum resulting from an arbitrary admixture of seed polarizations can be obtained by linear superposition.

The angular distribution of the seed photons.—We assume that the emitting surface is homogeneous. The output pulse profiles

and pulsed fractions depend more sensitively on the surface temperature distribution than does the high-energy tail of the X-ray spectrum. We wish to define the pulse profile shapes that can result from radiative transport in a current-carrying magnetosphere and the maximum pulsed fractions that can be obtained without resorting to temperature inhomogeneities across the surface.

The ratio of the seed photon energy to the cyclotron energy of the scattering charges at the magnetic pole, e.g., $k_B T_{bb}(\hbar |Ze| B_{pole}/mc)^{-1}$.—Although $|Ze|$, B_{pole}, and m are all independent quantities, they enter only in this ratio. One must, equivalently, specify the ratio of R_{NS} to $r_{bb} = R_{res}(\omega = k_B T_{bb}/\hbar)$ (eq. [6]),

$$\frac{R_{NS}}{r_{bb}} = \left(7 \times 10^{-2}\right)^{3/(2+p)} \left[\left(\frac{1}{|Z|}\frac{m}{m_e}\right)\frac{k_B T_{bb}}{0.4 \text{ keV}}\left(\frac{10^{14} \text{ G}}{B_{pole}}\right)\right]^{1/(2+p)}. \tag{18}$$

Because this ratio is small for electrons and positrons, in our calculation we inject photons moving in the radial direction from the surface of the star. The propagation of a nonradially moving photon would result in nearly radial propagation at the point of first scattering. We have checked (directly by simulation) that injecting the photons with a broad angular distribution results in practically identical spectra between ∼1 and ∼50 keV. A broader range of injection angles is also considered in the case of ion scattering (§ 4.5), where it is shown that there are modest differences in the output spectrum.

The momentum distribution f(p) of the charge carriers.—To explore the dependence of the results on $f(p)$, we use three distribution functions, which are taken to be independent of position:

1. A mildly relativistic flow in which the particle motion is restricted to one direction along the magnetic field (e.g., $\beta > 0$). We choose a one-dimensional Boltzmann distribution which is labeled by a temperature $k_B T_0 = (\gamma_0 - 1)m_e c^2$ or equivalently by a drift speed $\beta_0 = (1 - \gamma_0^{-2})^{1/2}$,

$$f(\beta\gamma) = \frac{1}{N_\beta K_1(1/(\gamma_0 - 1))} \exp\left[-\frac{\gamma}{\gamma_0 - 1}\right]$$
$$= \frac{1}{N_\beta K_1(1/(\gamma_0 - 1))} \exp\left[-\frac{\sqrt{1 + (\beta\gamma)^2}}{\gamma_0 - 1}\right], \tag{19}$$

where K_1 is the modified Bessel function and N_β is the number of directions in which the scattering particles move along the magnetic field. Here we write f as a distribution in momentum $\beta\gamma$, which is normalized in the usual manner,

$$\int_0^\infty d(\beta\gamma)f(\beta\gamma) = 1, \tag{20}$$

for the asymmetric distribution with $N_\beta = 1$.

2. A mildly relativistic, one-dimensional gas with the same Boltzmann distribution as type I, but now extending over positive and negative momenta, $-\infty < \beta\gamma < \infty$. In this case, the normalization of f is smaller by a factor of $N_\beta^{-1} = \frac{1}{2}$. This type of symmetric distribution plausibly describes an electron-positron gas. In the magnetospheric circuit, the positrons are identified with the half of the distribution function with positive velocity, and the electrons with the particles with negative velocity. (Both types of particle must exist in essentially equal numbers when the plasma is dominated by pairs, because it is nearly charge neutral.)

3. A broad power law in momentum,

$$f(\beta\gamma) \propto (\beta\gamma)^\alpha, \tag{21}$$

with minimum and maximum values $(\beta\gamma)_{min}$ and $(\beta\gamma)_{max}$, representing a warm relativistic plasma. The index $\alpha = -1$ corresponds to an equal number of particles per decade of momentum. We consider only distributions with $\alpha \leq 0$, since distributions with positive α are subject to vigorous kinetic instabilities (e.g., Kulsrud 2005).

These three families of distribution functions are characterized by the parameters $\{\beta_0\}$ for the Boltzmann distributions and by $\{\beta_{min}, \gamma_{max}, \alpha\}$ for the power-law distribution. In practice, the distribution functions are sampled only over a finite range of velocities, and upper and lower cutoffs are applied to the admissible values of β. For the distributions of type I and II, these cutoffs are taken to be very close to zero and unity, respectively. See § 3.4 for further details.

The particle distribution function must actually vary with position in the magnetosphere. A strong drag force acts on electrons and positrons at $r \sim 100$ km, where their cyclotron energy is in the keV range (Thompson & Beloborodov 2005). As a result, one expects the motion of the light charges to be mildly relativistic in this part of the magnetosphere. Published calculations of the charge dynamics in the closed magnetospheric circuit (Beloborodov & Thompson 2007) allow for pair creation, but do not model the outer part where $B < B_{QED}$. Close to the star, the particles have a broad relativistic distribution, extending up to an energy $\gamma_{res}m_e c^2 \sim \hbar e B_{pole}/m_e c k_B T_{bb}$ (Beloborodov & Thompson 2007). At this Lorentz factor, it is possible to spawn new electron-positron pairs through the excitation of a charge to its first Landau state by absorbing a photon from the peak of the thermal radiation field. Understanding the interplay between these two competing effects requires coupled radiation transfer and electrodynamic calculations, which we will pursue elsewhere.

3. MONTE CARLO SIMULATION

The random nature of photon scattering in the magnetosphere and the statistical character of observable quantities (spectra, pulse profiles) makes the Monte Carlo technique especially suitable. (See, e.g., Sobol' [1994] for an overview of Monte Carlo methods for Compton scattering in hot plasmas.) We now present the details of the magnetospheric model and the numerical algorithm. The results of our calculations are reported in § 4. Some validation tests are described in Appendix A.

3.1. *Transfer of Photons through a Cyclotron Scattering Atmosphere*

We now present the basic equations that describe the transfer of radiation through a cloud of particles with an arbitrary (relativistic) distribution function. A photon following a ray path $\boldsymbol{r} = \boldsymbol{r}_0 + \ell\hat{\boldsymbol{k}}$ sees a differential optical depth

$$\frac{d\bar{\tau}_{res}(\omega, \hat{\boldsymbol{k}}, \boldsymbol{r})}{d\ell} = \int_{-1}^1 d\beta \frac{dn_Z}{d\beta} \sigma_{res}(\omega, \hat{\boldsymbol{k}}, \boldsymbol{r}) \tag{22}$$

for cyclotron scattering. The point of emission of the photon is labeled by $\boldsymbol{r}_0$ ($\ell = 0$). The one-dimensional velocity $\beta\hat{\boldsymbol{B}}$ of the charges has the distribution

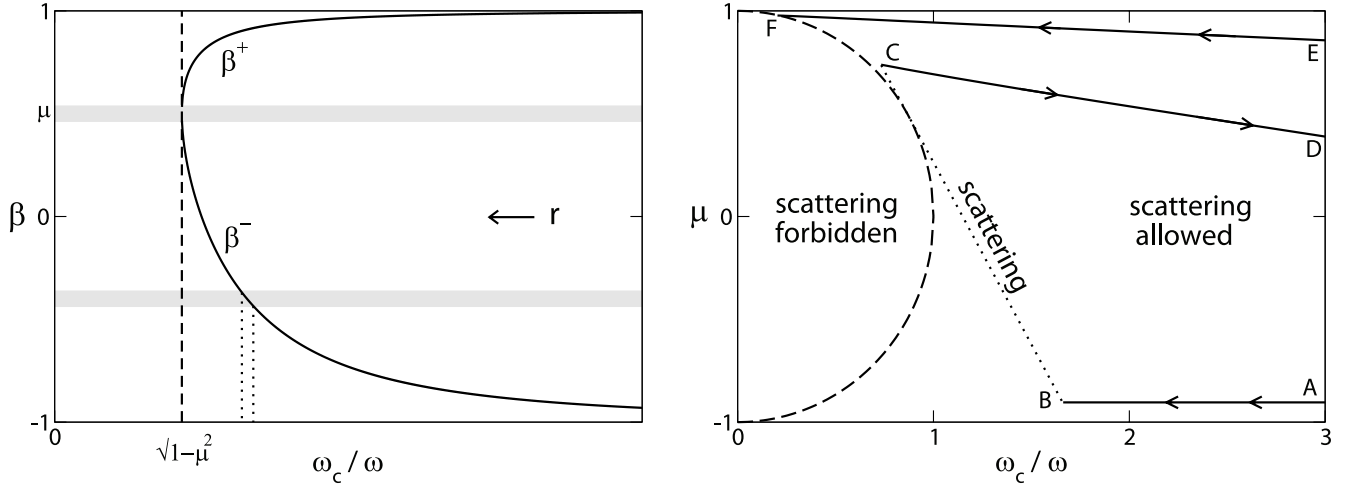$$f_Z(\beta, \boldsymbol{r}) = n_Z^{-1}\frac{dn_Z}{d\beta}, \tag{23}$$

FIG. 1.—*Left*: Solid curve denotes the velocities $\beta^{\pm}$ (eq. [26]) of the charges that are in resonance with a photon of frequency ω and direction cosine μ (as measured with respect to local magnetic field). The vertical dashed curve represents the escape surface, which is determined self-consistently by the condition $\omega_c/\omega = (1 - \mu^2)^{1/2}$ or equivalently by $\beta^{\pm} = \mu$ (see text). No resonant scattering is possible to the left of this line. When the velocity distribution of the charges is narrow (*horizontal shaded bars*), resonant scattering is possible only with a narrow range of ω_c/ω and of radius. This resonant surface is even narrower in coordinate and frequency space when it overlaps with the escape surface. *Right*: Sample photon trajectory in the (ω_c/ω)-μ plane. Here the escape surface is represented by the dashed curve $\mu^2 + (\omega_c/\omega)^2 = 1$. The photon trajectory starts at the surface of the star (to the extreme right, not shown), enters the plotted domain at point A, and scatters at point B. After the first scattering, the frequency and direction cosine of the photon shift over to point C. In the example shown, the photon is backscattered to smaller radius and leaves and reenters the plotted domain at points D and E, respectively. It finally escapes the magnetosphere at point F without any further scatterings.

where $\int_{-1}^{1} f_Z(\beta, \mathbf{r})\, d\beta = 1$. Given that particles of charge Ze carry a fraction ε_Z of the current, their space density n_Z can be obtained from equation (4),

$$\frac{|Z|en_Z}{B} = \varepsilon_Z \frac{(p+1)}{4\pi r |\beta|} \frac{B_\phi}{B_\theta}. \tag{24}$$

We focus on a single species of scattering charge in the remainder of this section and drop the subscript Z. Radiation transfer through an electron-positron plasma is easily described by writing $n = n_- + n_+$ and $f(\beta, \mathbf{r}) = f_-(\beta, \mathbf{r}) + f_+(\beta, \mathbf{r})$, where the subscript labels the sign of the charge. We treat the effects of ions and electrons separately in the case of an electron-ion plasma. In the formulae below, the factor ε represents the fraction of the current that is carried by the *scattering* charges; $\varepsilon = 1$ for a pure pair plasma. Substituting equations (13), (23), and (24) into equation (22) gives

$$\frac{d\bar{\tau}_{\mathrm{res}}}{d\ell} = \varepsilon \frac{\pi(p+1)}{r} \left(\frac{B_\phi}{B_\theta} \right)$$
$$\times \left[\int_{-1}^{1} \frac{(1 - \beta\mu)|e'_{l,r}|^2}{|\beta|} \omega_D \delta(\omega - \omega_D) f(\beta, \mathbf{r})\, d\beta \right]. \tag{25}$$

At a given location in the magnetosphere, the resonance condition in equation (12) can be satisfied only for two values of β

$$\beta^{\pm}(\mathbf{r}, \hat{\mathbf{k}}, \omega) = \frac{1}{(\omega_c/\omega)^2 + \mu^2} \left[\mu \pm \frac{\omega_c}{\omega} \sqrt{\left(\frac{\omega_c}{\omega} \right)^2 + \mu^2 - 1} \right], \tag{26}$$

which depend on the photon frequency ω and propagation direction $\hat{\mathbf{k}}$ and the local cyclotron frequency ω_c. We can eliminate the delta function in equation (25) through the substitution

$$\delta(\omega - \omega_D) = \frac{\delta(\beta - \beta^{\pm})}{|\partial \omega_D/\partial\beta|_{\beta^{\pm}}}, \tag{27}$$

because ω_D is a function of β only for fixed $\mathbf{r}$, ω, and $\hat{\mathbf{k}}$. The velocity-averaged optical depth is then

$$\frac{d\bar{\tau}_{\mathrm{res}}}{d\ell} = \varepsilon \frac{\pi(p+1)\omega}{r} \left(\frac{B_\phi}{B_\theta} \right) \left[\frac{(1 - \beta^+\mu)|e'_{l,r}|^2_{\beta^+}}{|\beta^+|} \frac{f(\beta^+, \mathbf{r})}{|\partial\omega_D/\partial\beta|_{\beta^+}} \right.$$
$$\left. + \frac{(1 - \beta^-\mu)|e'_{l,r}|^2_{\beta^-}}{|\beta^-|} \frac{f(\beta^-, \mathbf{r})}{|\partial\omega_D/\partial\beta|_{\beta^-}} \right]. \tag{28}$$

Once the frequency and direction of the photon are fixed, the resonance condition can be expressed in terms of two functions $\beta^{\pm}$ of two local parameters ω_c/ω and μ. A narrow distribution of charges in velocity space implies the existence of a well-defined "resonant surface" in coordinate space (Fig. 1). (The shape of this resonant surface shifts with the direction of the photon if the charges are in bulk motion.) Resonant scatterings are possible only in a restricted part of this parameter space; equation (26) has solutions only if

$$\mu^2 + \left(\frac{\omega_c}{\omega} \right)^2 > 1. \tag{29}$$

The division of the photon trajectory into discrete steps, whose size is adapted according to a predetermined velocity distribution function, is the core of the Monte Carlo method used in this paper. The propagation of a photon through the magnetosphere is calculated most conveniently in this resonant velocity space; this allows the step size to be weighted appropriately by the density of the resonating charges. See Figure 1 (*left*) for an illustration. We neglect the effect of gravity on the photon trajectory, so that $\hat{\mathbf{k}}$ is constant in between scatterings. Applying the resonance condition $\omega_D = \omega$ (eq. [12]) gives

$$d\omega_D = \left(\frac{\omega_D}{B} \frac{dB}{d\ell} + \frac{\partial\omega_D}{\partial\mu} \frac{d\mu}{d\ell} \right) d\ell + \frac{\partial\omega_D}{\partial\beta} d\beta = 0, \tag{30}$$

where $dB/d\ell = \nabla B \cdot \hat{k}$ and $d\mu/d\ell = \nabla\mu \cdot \hat{k}$. The relation between the step size in coordinate space and in velocity space becomes

$$\Delta\ell = -\frac{(\partial\omega_D/\partial\beta)_{\beta^\pm}}{(\partial\omega_D/\partial\ell)_{\beta^\pm}}\Delta\beta^\pm, \qquad (31)$$

where

$$\frac{1}{\omega_D}\frac{\partial\omega_D}{\partial\ell} = \frac{1}{B}\frac{dB}{d\ell} + \frac{\beta}{(1-\beta\mu)}\frac{d\mu}{d\ell}. \qquad (32)$$

The differential optical depth is then

$$\Delta\bar{\tau}_{\rm res} = \varepsilon\frac{\pi(p+1)\omega}{r}\left(\frac{B_\phi}{B_\theta}\right)\left[\frac{(1-\beta^+\mu)|e'_{l,r}|^2_{\beta^+}}{|\beta^+|(\partial\omega_D/\partial\ell)_{\beta^+}}f(\beta^+)\,\Delta\beta^+ \right.$$
$$\left. -\frac{(1-\beta^-\mu)|e'_{l,r}|^2_{\beta^-}}{|\beta^-|(\partial\omega_D/\partial\ell)_{\beta^-}}f(\beta^-)\,\Delta\beta^-\right]. \qquad (33)$$

The two terms in equation (33) have opposite signs, because the two branches of $\beta^\pm$ advance in opposite directions in velocity space for a given photon direction in coordinate space (see Fig. 1, *left*). When substituting equation (31) into equation (28), we get a factor

$$\left(\frac{\partial\omega_D/\partial\beta}{|\partial\omega_D/\partial\beta|}\right)_{\beta^\pm} = \frac{\mu-\beta^\pm}{|\mu-\beta^\pm|}, \qquad (34)$$

which is +1 for β^- and −1 for β^+. The gradient of the Doppler-shifted cyclotron frequency (eq. [32]) is generally dominated by the gradient in magnetic field strength and is negative for photons moving away from the star.

The photon step size $\Delta\ell$ can be chosen in such a way that the products $f(\beta^\pm, r)\Delta\beta^\pm$ (as determined from eq. [31]) yield a small value for $\Delta\bar{\tau}_{\rm res}$. This method ensures that the bulk of the resonant surface [where $f(\beta^\pm, r)$ is high] is traversed with a small step size.

3.2. Photon Escape from the Magnetosphere

A photon cannot resonantly scatter in the outer region where $\mu^2 + (\omega_c/\omega)^2 < 1$ (see eqs. [26] and [29]). This inequality is a sufficient condition, which is independent of the velocity distribution of the charges. Nonetheless, it is possible for a photon to leave and then reenter the inner region where resonant scattering is allowed. To see this, it is easiest to examine the photon trajectories in the (ω_c/ω)-μ plane (Fig. 1, *right*). The trajectories are generally not straight lines in this plane, but have a mild curvature close to the escape surface, as long as no scattering occurs.

We therefore adopt a second criterion, which must be satisfied if a photon in a Monte Carlo simulation can be considered to have entirely escaped the star and become observable. The tangent vector of the photon trajectory in the (ω_c/ω)-μ plane,

$$t = \left(\frac{\omega_c}{\omega}\right)\frac{1}{B}\frac{dB}{d\ell}\hat{\omega} + \frac{d\mu}{d\ell}\hat{\mu}, \qquad (35)$$

must not point in a direction that intersects the escape surface for a second time. [Here the unit vector $\hat{\omega}$ runs parallel to the (ω_c/ω)-axis.] In other words, we require that t points in the direction of the line segment $(\omega_c/\omega) = 0$, $-1 < \mu < 1$ that forms the left boundary of the (ω_c/ω)-μ plane. If this condition is not satisfied in combination with $\mu^2 + (\omega_c/\omega)^2 < 1$, then it is necessary

to follow the photon trajectory to check whether it reenters the region where resonant scattering is allowed.

A special case occurs for monopolar fields and photons emitted very near the magnetic poles in a dipole field. In both these cases, the photon trajectory will tend to $\mu = \pm 1$ at large distances from the star. In numerical calculations an arbitrary cutoff needs to be taken. In our model, this is not a problem for dipole-like fields, since the optical depth vanishes at the magnetic poles (recall eq. [4]).

The curvature of the resonant surface plays an important role in determining the rate of photon escape. Consider the case in which $\beta^\pm \simeq \mu$, so that the resonant surface of a photon overlaps its escape surface. For the purpose of illustration, imagine a top-hat velocity distribution that is independent of position and has a narrow width $\Delta\beta$ centered about $\beta = \bar{\beta}$,

$$f(\beta,\bar{\beta},\Delta\beta) = \begin{cases} \dfrac{1}{\Delta\beta}, & \left(\bar{\beta}-\dfrac{\Delta\beta}{2}\right) < \beta < \left(\bar{\beta}+\dfrac{\Delta\beta}{2}\right), \\ 0, & \text{otherwise.} \end{cases} \qquad (36)$$

Two such distribution functions are depicted as horizontal shaded bars in Figure 1 (*left*). If $\bar{\beta}$ happens to be very different from μ (the lower example), then the resonant surface has a width

$$\frac{\Delta r}{r} \simeq \Delta\beta\left|\frac{d\ln B}{d\ln r}\right|^{-1}, \qquad (37)$$

which depends on $\Delta\beta$. But if $\bar{\beta} - \frac{1}{2}\Delta\beta < \mu < \bar{\beta} + \frac{1}{2}\Delta\beta$, then the resonant surface becomes very thin in the radial direction and relatively thick in the nonradial direction. The distance over which the photon escapes from the resonant layer then depends on the rate at which the layer curves away from the photon trajectory.

In practice, enough photons are scattered into an angle $\mu \simeq \bar{\beta}$ that the transport of photons through a resonant layer is not well approximated by a one-dimensional model (e.g., a model in which the cyclotron frequency has a gradient only perpendicular to the resonant surface: Zheleznyakov 1996; Lyutikov & Gavriil 2006). In this situation, the step size has to be reduced appropriately (see § 3.3).

3.3. Code Description: Single Photon Evolution

We evolve a single photon at a time, from the point of emission on the neutron star surface to the final escape (as defined by the criteria § 3.2). The final frequency $\omega_{\rm out}$ and direction cosine μ_k relative to the magnetic axis are then recorded. This process is repeated until the distributions in $\omega_{\rm out}$ and μ_k are well sampled, according to criteria discussed in Appendix A.

In our code, a photon is a seven-dimensional vector, the components of which are its position r, direction $\hat{k}$, frequency ω, and polarization (E or O).[5] Although the photon's electric vector is defined with respect to the local magnetic field, the polarization will adjust adiabatically as the photon propagates through the magnetosphere.[6] The code is implemented in FORTRAN 77.

---

[5] The photon's position and direction are defined in a spherical coordinate system centered on the star: $r = (r, \cos\theta = \hat{r}\cdot\hat{z}, \phi)$ and $\hat{k} = (\mu_k = \hat{k}\cdot\hat{z}, \phi_k)$. Here $\hat{z}$ runs parallel to the star's magnetic axis. Our unit of frequency is $\omega_{\rm bb} = k_B T_{\rm bb}/\hbar$, of magnetic field $B_{\rm bb} = mc\omega_{\rm bb}/(|Z|e)$, and of length $r_{\rm bb} = R_{\rm res}(\omega_{\rm bb})$ (eq. [18]).

[6] The polarization tracking of an X-ray photon breaks down only outside the last surface of cyclotron scattering.
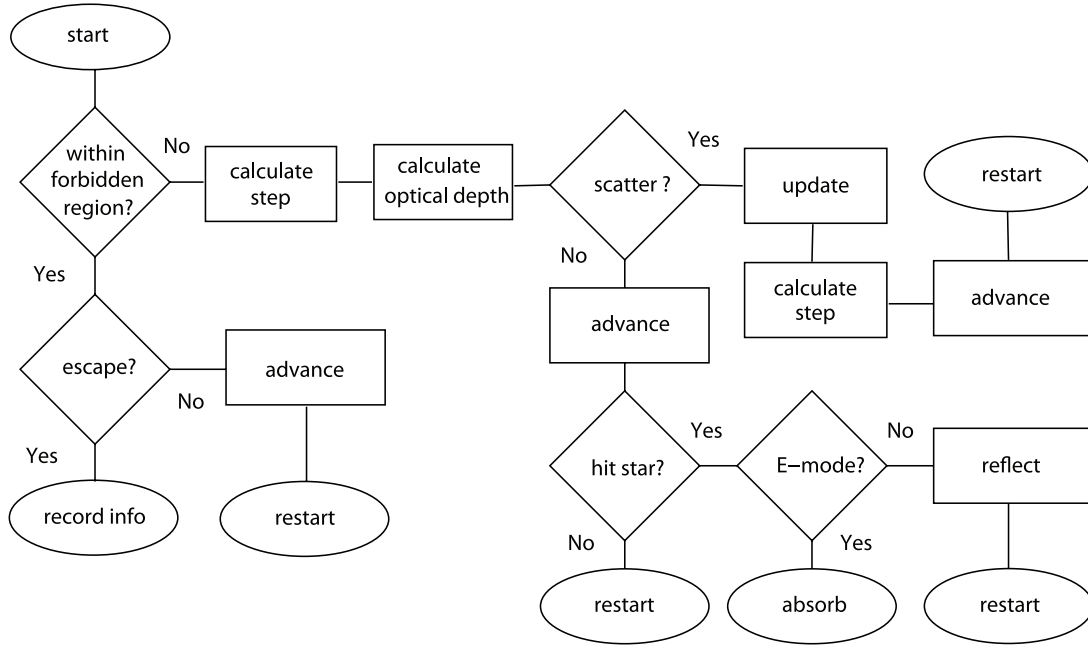
Fig. 2.—Flow chart showing evolution of single photon. Ellipses contain starting, ending, and loop points in the algorithm, diamonds contain decision points, and rectangles contain simple instructions. See text for a detailed explanation.

Each photon is injected at a random point on the stellar surface, $r = R_{\rm NS}$, with a wavevector pointing in the radial direction, with a frequency drawn from a given input spectrum, and with fixed polarization. Once the initial ray path is chosen, the photon's position and frequency are updated through a set of binary decisions; see the flowchart in Figure 2.

First, we check whether the escape criteria defined in § 3.2 are satisfied. If the photon must escape, its frequency ω and direction angles μ_k and ϕ_k are recorded. (The magnetic field is axisymmetric in the calculations presented in this paper, and ϕ_k is not used in the analysis.)

Second, the subsequent step size along the photon's trajectory is determined by an adaptive algorithm (§ 3.4) that minimizes the step size in regions where the density of resonating charges is highest. The step size is further reduced whenever $\beta^{\pm} \simeq \mu$, until the condition

$$\frac{\Delta|\mu - \beta|}{|\mu - \beta|} < 10^{-2} \qquad (38)$$

is satisfied.

If the photon does not escape immediately, then we determine whether it scatters by drawing a random number (§ 3.4). The contributions of the two resonant populations of charges $\beta^{\pm}$ are included in the calculation of the differential optical depth. If the photon scatters, then its vector is updated. A new value for the step size is calculated, the photon is advanced, and the loop is restarted.

If the photon does not scatter, we advance it one step. Before restarting the loop, we check whether it hits the stellar surface. An E-mode photon that hits the surface is assumed to be absorbed; its nonresonant opacity is strongly suppressed, so the photon penetrates to a depth where the absorption opacity dominates over scattering. Such a photon does not contribute to the output spectrum, and only its absorption is recorded. We allow half of the O-mode photons hitting the star to scatter elastically off the surface and half to be absorbed.

Each photon is assumed to propagate on a straight line, and the effect of gravitational light bending close to the star is ignored. This approximation is excellent near the first resonant scattering surface if the scattering charge is an electron or positron, since $r_{\rm res} \gg 2GM_{\rm NS}/c^2 \sim R_{\rm NS}/3$ (see eq. [6]), where $M_{\rm NS}$ is the neutron star mass. The temperature is assumed to be constant over the stellar surface, so the effects of light bending can be neglected closer to the star. Light bending is more important when the ions are the dominant source of opacity in the magnetosphere (as they may be in the period of strong afterglow following SGR bursts; Ibrahim et al. 2001). We present some preliminary results for ion scattering in § 4.5. The combined effect of light bending and surface temperature variations will be included in future calculations.

This Monte Carlo procedure is independent of the magnetic field geometry and velocity distribution function, as long as only one species of scattering particle is involved. It can easily be generalized to include multiple scattering species and multipeaked velocity distribution functions (electron-positron pairs).

3.4. Adaptive Step Size Algorithm

The evolution of a photon's position is performed in velocity space for type I and II distributions and in momentum space for type III (§ 2.3). To maximize accuracy and minimize computing time, larger steps are taken when $f(\beta^{\pm}, r)$ is small and vice versa.

To implement this approach, we assume that any velocity distribution at a given position r can be characterized by a single peak with half-widths $\Delta\beta_{\rm low}$ and $\Delta\beta_{\rm high}$ centered at $\beta = \bar{\beta}$. In the case of a broad distribution, we take the median value of β as the central point. In the case where the distribution function is supported over a range of β extending downward to 0 or upward to unity (e.g., the Boltzmann distribution), we restrict the values of β at the extremes of this range to avoid numerical problems. The limits are chosen empirically so that the output spectra and pulse profiles are insensitive to the choice. In practice, this involves sampling some 99.8% of the (integrated) distribution function, so that $\int_0^{\beta_{\rm min}} f(\beta)\, d\beta = \int_{\beta_{\rm max}}^1 f(\beta)\, d\beta = 0.001$. Thus, if both β^+

and β^- are outside the resonant region, we take a big step in coordinate space ($\Delta \ell = r/10$). If the value of either β^+ or β^- is approaching a possible resonance, we refine the step in velocity/momentum space until the edge of the region is resolved to a fiducial accuracy, namely, $\Delta\beta_{\rm low/high}/100$. Finally, if either of them lies within the resonance surface, we set the step to a small logarithmic increment in momentum space,

$$d(\gamma\beta)_{\rm new} = {\rm sgn}\,[d(\gamma\beta)_{\rm old}]|\gamma\beta|/100, \qquad (39)$$

or equivalently, $d\beta_{\rm new} = {\rm sgn}\,(d\beta_{\rm old})(1-\beta^2)|\beta|/100$, where the subscripts old and new refer to the step size before and after refining, respectively, and sgn is the sign function. The numerical factor was calibrated empirically to ensure reasonable smoothness in the angular distributions of all cases explored. For the special case $\beta^\pm = 0$, we set the step to a small constant. Once the appropriate size of the step in either coordinate or velocity space has been determined, the complete set of steps ($\Delta \ell, \Delta\beta^+$, and $\Delta\beta^-$) is determined from equation (31).

The differential optical depth in equation (33) is calculated by separating the contributions of the two resonant populations β^+ and β^- of particles, $\Delta\bar{\tau}_{\rm res} = \Delta\bar{\tau}_{\rm res}^+ + \Delta\bar{\tau}_{\rm res}^-$. Next we generate a uniformly distributed random number $\mathcal{R}$ in the range $[0, 1]$. If $\mathcal{R} < (1 - \exp\,[\Delta\bar{\tau}_{\rm res}])$, the photon scatters, in which case the new direction angles and frequency are calculated according to the method described in § 3.5. In the case when both $\Delta\bar{\tau}_{\rm res}^+$ and $\Delta\bar{\tau}_{\rm res}^-$ are nonzero, the value of β used for scattering is chosen by generating a new random number $\mathcal{R}_1$; if $\mathcal{R}_1 < \Delta\bar{\tau}_{\rm res}^+/\Delta\bar{\tau}_{\rm res}$, the photon scatters with β^+, otherwise it scatters with β^-.

3.5. *Choice of New Photon Direction after Scattering*

The direction cosine of the photon is chosen randomly in the rest frame[7] of the scattering particle, with a weighting appropriate to the particular scattering process. We use a similar approach to calculate the surface reflection of an O-mode photon.

The differential cross section for resonant cyclotron scattering into *both* polarization modes is proportional to (e.g., Wang et al. 1988)

$$\frac{d\sigma_{\rm res}}{d\mu'd\alpha} \propto 1 + \mu'^2, \qquad (40)$$

where $\mu' = \hat{\boldsymbol{B}} \cdot \hat{\boldsymbol{k}}$ is the direction cosine of the outgoing photon in the rest frame of the scattering particle and α is its azimuthal angle about the local magnetic field direction. The cumulative probability of scattering into an angle less than or equal to μ' is then

$$P(\mu') = \frac{1}{8}\left(\mu'^3 + 3\mu' + 4\right). \qquad (41)$$

We set P equal to a uniformly distributed random number in the range $[0, 1]$ and then solve for the value of μ'. The direction cosine μ of the photon in the frame of the star is obtained from equation (17), since the resonant value of β is known.

The polarization of the outgoing photon is then determined by drawing a second random number in the range $[0, 1]$; the outgoing photon is in the E-mode if this number is smaller than $(1 + \mu'^2)^{-1}$ and is in the O-mode otherwise.

The azimuthal angle α is uniformly distributed between 0 and 2π; we take the zero of α to coincide with the $\hat{\boldsymbol{B}}$-$\hat{\boldsymbol{z}}$ plane (see

[7] Throughout this subsection, the prime labels the photon after scattering.
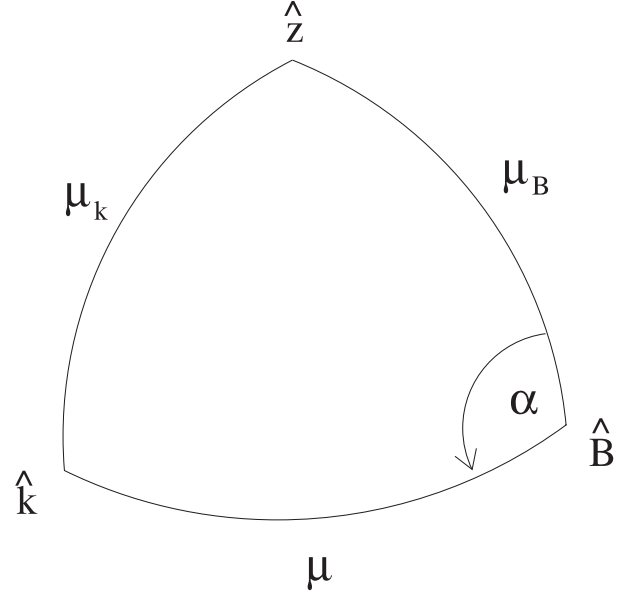
FIG. 3.— Angles defined at a scattering site in the stellar frame. The vectors $\hat{\boldsymbol{z}}$, $\hat{\boldsymbol{B}}$, and $\hat{\boldsymbol{k}}$ correspond to the directions of the magnetic axis, the local magnetic field, and the photon wavevector, respectively. See text for the definition of other quantities.

Fig. 3). The angle $\mu_B = \hat{\boldsymbol{B}} \cdot \hat{\boldsymbol{z}}$ is known from the position and magnetic field geometry. We then find the magnetic polar angle μ_k of the outgoing photon using the cosine theorem for spherical triangles,

$$\mu_k = \mu_B\mu + \sqrt{(1 - \mu_B^2)(1 - \mu^2)}\cos\alpha. \qquad (42)$$

To find the azimuthal angle ϕ_k about the magnetic axis of the star, we solve for the Cartesian components k_x, k_y, and k_z, using the system of equations

$$k_z = \mu_k, \qquad (43)$$

$$\hat{\boldsymbol{k}} \cdot \hat{\boldsymbol{B}} = \mu, \qquad (44)$$

$$\hat{\boldsymbol{k}} \cdot (\hat{\boldsymbol{B}} \times \hat{\boldsymbol{z}}) = \sqrt{(1 - \mu_B^2)(1 - \mu^2)}\sin\alpha. \qquad (45)$$

This gives $\phi_k = \arctan\,(k_y/k_x)$.

3.6. *Statistical Treatment of Recorded Data*

The state of each escaping photon is defined by its frequency ω and direction cosine μ_k relative to the magnetic axis. (The magnetosphere and photon source are axially symmetric, so we ignore the azimuthal angle ϕ_k.)

Care must be taken in choosing the frequency distribution of the seed photons. It is straightforward to draw directly from a blackbody number distribution

$$B\left(\log\frac{\omega_{\rm in}}{\omega_{\rm bb}}\right) = \frac{dN}{d\log\,(\omega_{\rm in}/\omega_{\rm bb})} \propto \frac{(\omega_{\rm in}/\omega_{\rm bb})^3}{\exp\,(\omega_{\rm in}/\omega_{\rm bb}) - 1}, \qquad (46)$$

where $\omega_{\rm in}/\omega_{\rm bb}$ is the input frequency in units of $\omega_{\rm bb} \equiv k_B T_{\rm bb}/\hbar$. However, it is difficult to obtain good sampling of this distribution at very low and very high frequencies, because it drops off rapidly at $\omega \ll \omega_{\rm bb}$ and $\omega \gg \omega_{\rm bb}$.

We therefore adopt an alternative procedure; we use the same input frequency for all the photons and store the output frequencies and direction angles in a normalized response function

$$R\left(\log\frac{\omega_{\text{out}}}{\omega_{\text{in}}}, \mu_k\right) = \frac{1}{N_{\text{phot}}} \frac{dN}{d\mu_k \, d\log\left(\omega_{\text{out}}/\omega_{\text{in}}\right)}, \quad (47)$$

where $\omega_{\text{out}}/\omega_{\text{in}}$ is the frequency shift relative to the input frequency and N_{phot} is the total number of photons. The outgoing histogram in frequency and direction is then

$$H\left(\log\frac{\omega_{\text{out}}}{\omega_{\text{bb}}}, \mu_k\right)$$
$$= \int R\left(\log\frac{\omega_{\text{out}}}{\omega_{\text{in}}}, \mu_k\right) B\left(\log\frac{\omega_{\text{in}}}{\omega_{\text{bb}}}\right) d\log\frac{\omega_{\text{in}}}{\omega_{\text{bb}}}, \quad (48)$$

which is a convolution in $\log\omega$. The underlying assumption in this procedure is that the outgoing distribution in μ_k is independent of frequency, which certainly holds for the self-similar field geometry, but not for more complicated field geometries with multipolar structure. The drawback of this approach is that by choosing a single input frequency, one implicitly fixes the initial scattering radius (which depends on frequency) relative to the stellar radius. Nevertheless, since most photons are emitted at frequencies near the blackbody peak, excellent accuracy is obtained by choosing the peak frequency

$$\omega_{\text{in}} = \omega_{\text{peak}} \equiv 2.82144\left(\frac{k_B T_{\text{bb}}}{\hbar}\right) \quad (49)$$

as the input frequency. In Appendix A we describe validation runs that confirm that this procedure produces results very close to those obtained by drawing frequencies directly from the blackbody distribution.

The response function R is normalized to unity (modulo the small effect of photon reabsorption at the surface), because the total number of photons is conserved by scattering. The upscattering of photons in frequency therefore implies a transfer of kinetic energy from the charges to the photons, which ultimately is drawn from the energy stored in the external toroidal field (Thompson et al. 2002; Beloborodov & Thompson 2007).

We now show how pulse profiles and line-of-sight dependent spectra can be obtained from the function H. The energy flux at a fixed magnetic polar angle and in a fixed band $\omega_{\text{min}} < \omega < \omega_{\text{max}}$ is obtained by integrating H over frequency,

$$\frac{dF}{d\mu_k} = \int_{\omega_{\text{min}}}^{\omega_{\text{max}}} \hbar\omega H(\omega, \mu_k) \, d\log\omega. \quad (50)$$

To simulate a pulse profile, we pick the angle θ_Ω between the rotation axis and the magnetic axis and the angle θ_{los} between the rotation axis and the line of sight. In a coordinate system that is frozen into the star and aligned with its magnetic axis, the rotation axis rotates in azimuth,

$$\phi_\Omega = -\Omega t. \quad (51)$$

To obtain an accurate pulse profile with minimal noise, we integrate the energy flux over a beam of a finite angular width $\theta_{\text{beam}} = \cos^{-1}\mu_{\text{beam}}$ that is centered on the direction $\hat{\boldsymbol{O}}$ to the fiducial observer,

$$F_\Omega = \frac{1}{2\pi} \int_0^{2\pi} \int_{-1}^1 \frac{dF}{d\mu_k} \Theta(\hat{\boldsymbol{r}}' \cdot \hat{\boldsymbol{O}} - \mu_{\text{beam}}) d\mu' \, d\phi', \quad (52)$$

where Θ is the step function. The band energy flux so constructed depends only on the rotational phase ϕ_Ω and the orientation angles θ_Ω and θ_{los}. The angular integral in equation (52) is performed most easily in an inertial coordinate system that is aligned with the rotation axis and in which $\hat{\boldsymbol{O}} = (\theta_{\text{los}}, 0)$. Each point $\hat{\boldsymbol{r}}' = (\cos^{-1}\mu', \phi')$ in the integral must be related to the magnetic coordinate system,

$$\mu_k = \mu_\Omega\mu' + \sqrt{\left(1 - \mu_\Omega^2\right)\left(1 - \mu'^2\right)} \cos(\phi_\Omega - \phi'), \quad (53)$$

and to the observer's direction,

$$\hat{\boldsymbol{r}}' \cdot \hat{\boldsymbol{O}} = \mu_{\text{los}}\mu' + \sqrt{\left(1 - \mu_{\text{los}}^2\right)\left(1 - \mu'^2\right)} \cos\phi'. \quad (54)$$

In these expressions,

$$\mu_{\text{los}} = \cos\left(\theta_{\text{los}}\right), \quad \mu_\Omega = \cos\left(\theta_\Omega\right). \quad (55)$$

The rotationally averaged spectrum is obtained by removing the frequency integral and then integrating over the rotational phase,

$$\omega F_\omega = \frac{1}{(2\pi)^2}\bigg\{ \int_0^{2\pi} \int_0^{2\pi} \int_{-1}^1 \hbar\omega H(\omega, \mu_k)$$
$$\times \Theta(\hat{\boldsymbol{r}}' \cdot \hat{\boldsymbol{O}} - \mu_{\text{beam}}) d\mu' \, d\phi' \, d\phi_\Omega \bigg\}. \quad (56)$$

4. RESULTS

Our main goal in this paper is to determine the basic types of nonthermal spectra and pulse profiles that result from the transfer of X-ray photons through the scattering corona of a magnetar. To this end, we consider only the simplest distribution of seed photons, a single temperature blackbody, and the simplest example of a twisted magnetosphere, the self-similar sequence from equation (2) with a magnetic pitch angle that is independent of radius. We only make qualitative comparisons of our calculations to the observed population of SGRs and AXPs. For example, features in individual pulse profiles that are not reproduced by our calculations could plausibly indicate the presence of hotspots on the stellar surface or some nonaxisymmetry in the current flowing out to ~100 km from the star. We are able to reproduce the 1–10 keV pulsed fractions that are seen in all but one source (1E 1048.1−5937; Tiengo et al. 2005).

We do explore in some detail how the X-ray spectra and pulse profiles depend on the momentum distribution $f(p)$ of the magnetospheric particles. We consider the two basic types of distribution functions itemized in § 2.3: the relativistic Boltzmann distribution (eq. [19]) and a broad, power-law distribution in momentum (eq. [21]). We also perform some test calculations (Appendix A) with a top-hat velocity distribution from equation (36). We explore a range of mean drift speeds and power-law indices and also vary the magnetospheric twist angle $\Delta\phi_{\text{N-S}}$ (eq. [1]) and the orientation angles μ_Ω and μ_{los} (eq. [55]). The scattering charges are taken to have the charge/mass ratio of the electron, with the exception of the simulations of ion scattering presented in § 4.5. The results depend weakly on whether the photons are injected in the E-mode or O-mode (§ 4.6).

4.1. A Simple Model of a Blackbody + High-Energy Power Law

The X-ray spectra of the AXPs can be fitted by a superposition of a blackbody and a power law, with a photon index in the
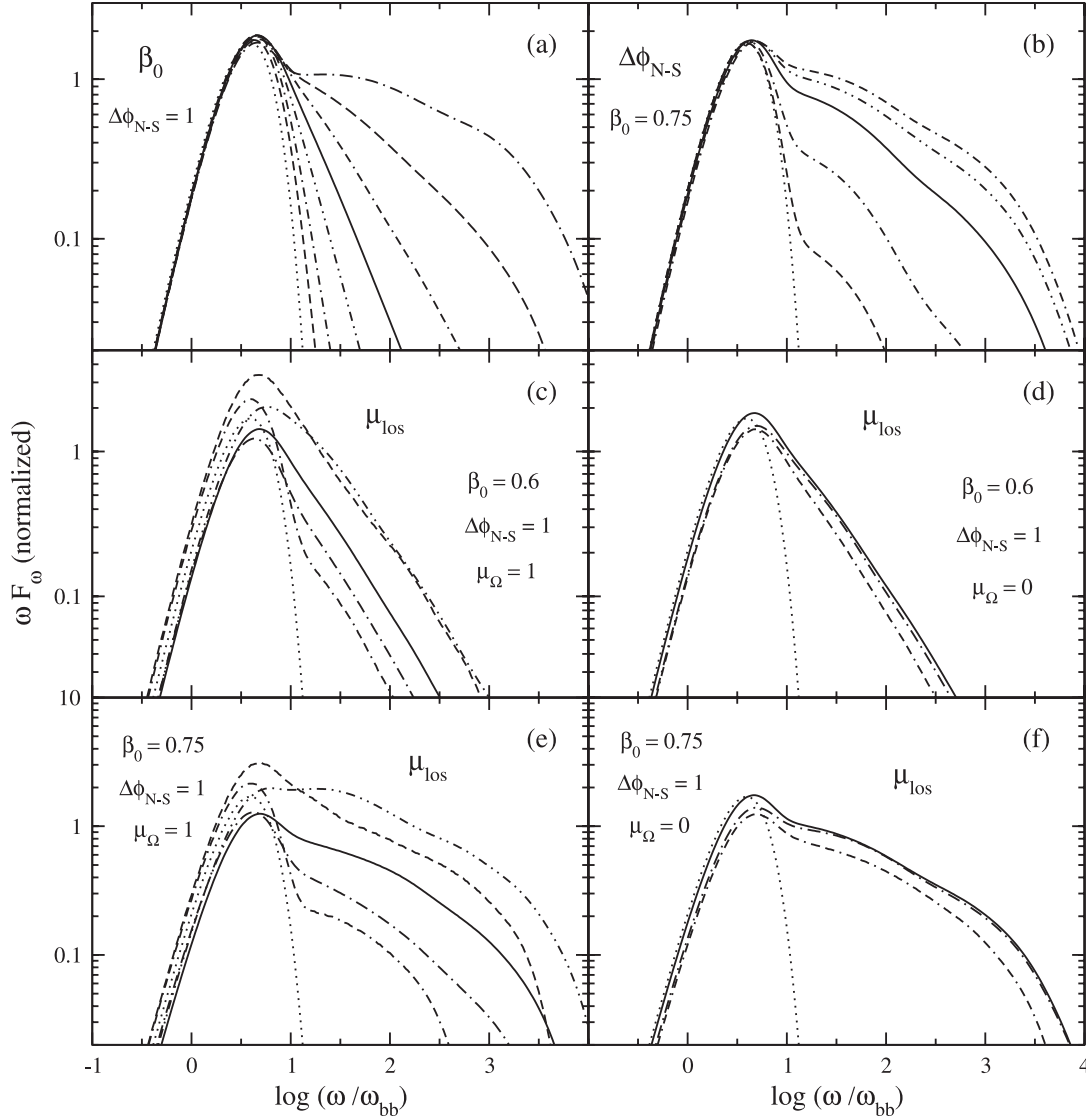
FIG. 4.—Energy spectra obtained with a unidirectional Boltzmann particle distribution (type I; eq. [19]). The unit of frequency is $\omega_{bb} = k_B T_{bb}/\hbar$, where the blackbody temperature T_{bb} is left arbitrary. The dotted curve denotes a Planck function of temperature T_{bb}, with a unit normalization below the curve. Curves in panel (a) correspond to different velocity spreads, with β_0 increasing from softest to hardest spectra, $\beta_0 = 0.2, 0.3, 0.4, 0.5, 0.6, 0.7$, and 0.8. All curves assume that $\Delta\phi_{N-S} = 1$ and that the magnetic axis and line of sight are both orthogonal to the rotation axis ($\mu_\Omega = \mu_{los} = 0$). Curves in panel (b) correspond to different twist angles, with $\Delta\phi_{N-S}$ increasing from softest to hardest spectra, $\Delta\phi_{N-S} = 0.1, 0.3, 0.7, 1$, and 1.3. Velocity spread $\beta_0 = 0.75$ is assumed and other parameters are as in (a). Changing the line-of-sight direction results in the spectra shown in panels (c)–(f): curves correspond to $\mu_{los} = 1$ (*dash-dash-dotted curve*), $1/\sqrt{2}$ (*dot-dashed curve*), 0 (*solid curve*), $-1/\sqrt{2}$ (*dot-dot-dashed curve*), and -1 (*dashed curve*). Panels (c) and (e) correspond to an aligned rotator ($\mu_\Omega = 1$), and panels (d) and (f) to an orthogonal rotator. Other parameters are the same as in panel (a). Photon indices obtained by fitting a blackbody plus power-law function in the frequency range $\log(\omega/\omega_{bb}) = 0.7$–1.4 are listed in Table 1.

range[8] $\Gamma = 2$–4 (Woods & Thompson 2006). Although a single power law typically provides a good fit to persistent SGR spectra, the Galactic SGR sources are more distant than the AXPs, and their spectra are more heavily absorbed. A blackbody component is present during transient X-ray afterglows that are observed following bursts of intermediate energy (e.g., Ibrahim et al. 2001) and in the persistent X-ray emission of SGR 1900+14 (Esposito et al. 2007).

In AXP spectra, the thermal and nonthermal components usually have a similar normalization at an energy of 1 keV. In other words, the power-law component pivots about the blackbody

peak, a behavior that was observed directly during a ~1 day X-ray outburst of 1E 2259+586 (Woods et al. 2004). Within that outburst, which produced more than 100 SGR-like bursts of subsecond duration, the high-energy photon index was observed to decay from $\Gamma = 2$ to 3.5.

This behavior suggests that the high-energy extension of the blackbody peak in the X-ray spectrum is created by upscattering the thermal photons in a corona above the surface of the neutron star. The model examined in this paper has this property. It also has the advantage that no fine tuning is required for the optical depth of the scattering charges or their mean energy. The optical depth is close to unity if the magnetosphere (or, more precisely, the part of the magnetosphere 100 km distant from the magnetar surface) is twisted.

---

[8] The photon index Γ is defined by $dN/d\omega \propto \omega^{-\Gamma}$, where $dN/d\omega$ is the number of photons emitted per unit frequency.
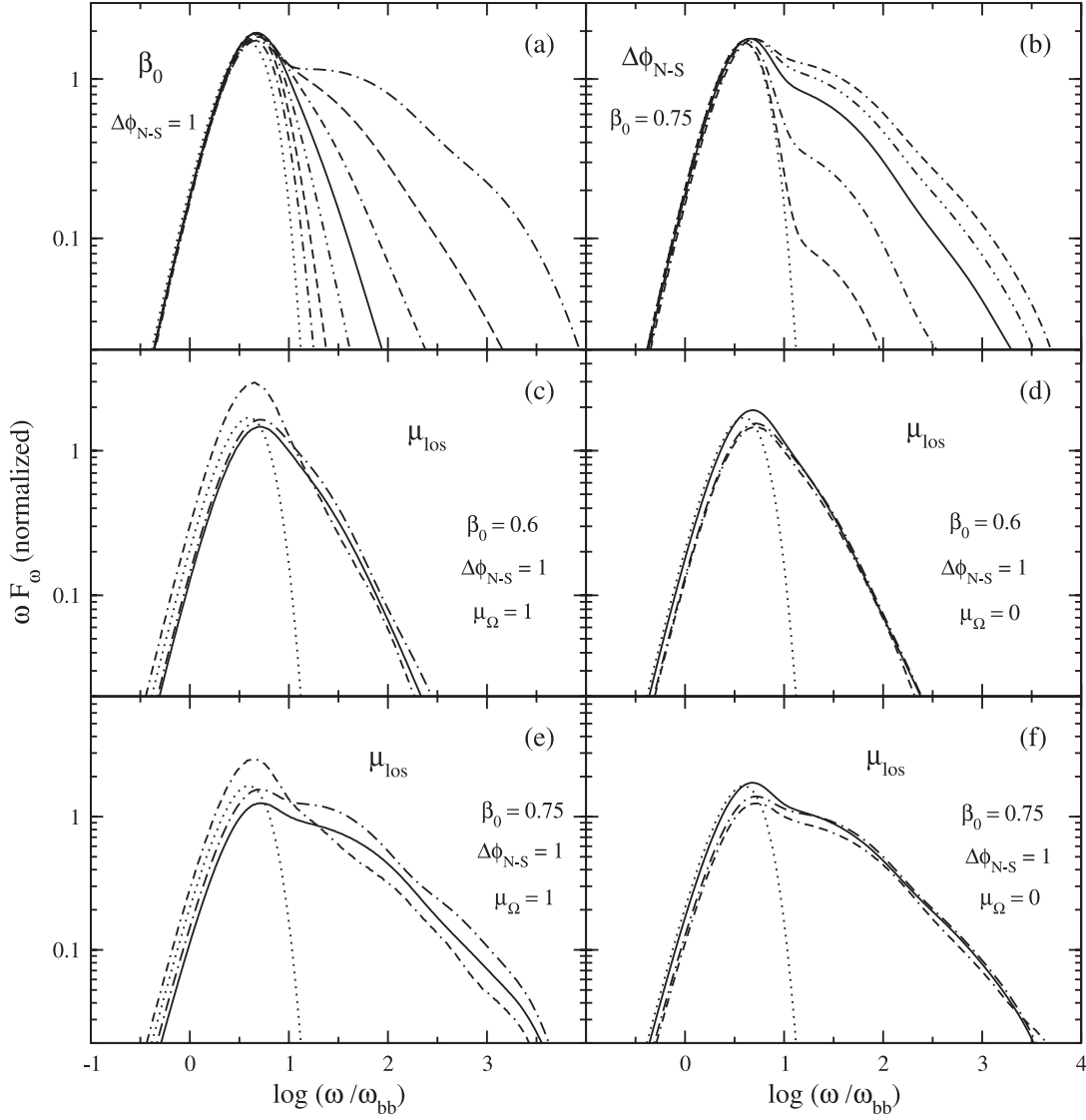
FIG. 5.—Same as Fig. 4, but for a distribution function that is bidirectional, corresponding to a pair plasma (type II; eq. [19]). In this case, there is a symmetry between positive and negative orientation angles μ_{los}, and curves are plotted only for $\mu_{\mathrm{los}} > 0$. Photon indices are listed in Table 2.

The standard blackbody + power-law fit to magnetar X-ray spectra fails to account for an important feature of our model: *the high-energy power-law component of the spectrum is not expected to continue below the blackbody peak*. This is not just an academic issue; in sources with relatively low extinctions, the power-law component dominates below the thermal peak and significantly biases the fit to the blackbody temperature (e.g., the AXP XTE J1810−197; Halpern & Gotthelf 2005).

This leads us to propose a simple generalization of the standard blackbody + power-law model. This model assumes that a fraction f_{uns} of the seed photons leaves the star without scattering, and the rest are upscattered following a power-law distribution (Appendix A). The angle-averaged response function, equation (47), can be written as

$$R\left(\log\frac{\omega_{\mathrm{out}}}{\omega_{\mathrm{in}}}\right) = f_{\mathrm{uns}}\,\delta\left(\log\frac{\omega_{\mathrm{out}}}{\omega_{\mathrm{in}}}\right)$$

$$+ f_{\mathrm{pl}}\,\Theta\left(\frac{\omega_{\mathrm{out}}}{\omega_{\mathrm{in}}} - 1\right)\left(\frac{\omega_{\mathrm{out}}}{\omega_{\mathrm{in}}}\right)^{\Gamma-1}, \quad (57)$$

where Θ is the step function. Using equations (46) and (48), we get

$$F_\omega^{\mathrm{fit}} = f_{\mathrm{uns}}\,B\left(\frac{\omega}{\omega_{\mathrm{bb}}}\right) + f_{\mathrm{pl}}\int_0^\omega B\left(\frac{\omega'}{\omega_{\mathrm{bb}}}\right)\left(\frac{\omega'}{\omega}\right)^{\Gamma-1}\frac{d\omega'}{\omega'}, \quad (58)$$

where $B(\omega/\omega_{\mathrm{bb}})$ is the Planck function, equation (46). Even though this behavior of the response function is seen only in simulations with a monoenergetic distribution function, equation (36), this generic fit worked relatively well for most of our results.[9]

4.2. Photon Index

Figures 4–6 show the energy spectra (ωF_ω) that result from choosing particle distribution functions of types I–III, respectively. The Planck function is plotted for comparison and is normalized to have a unit area. A high-energy excess above the

---

[9] This implies that f_{uns} is a fit parameter that may differ from the actual fraction of unscattered photons.
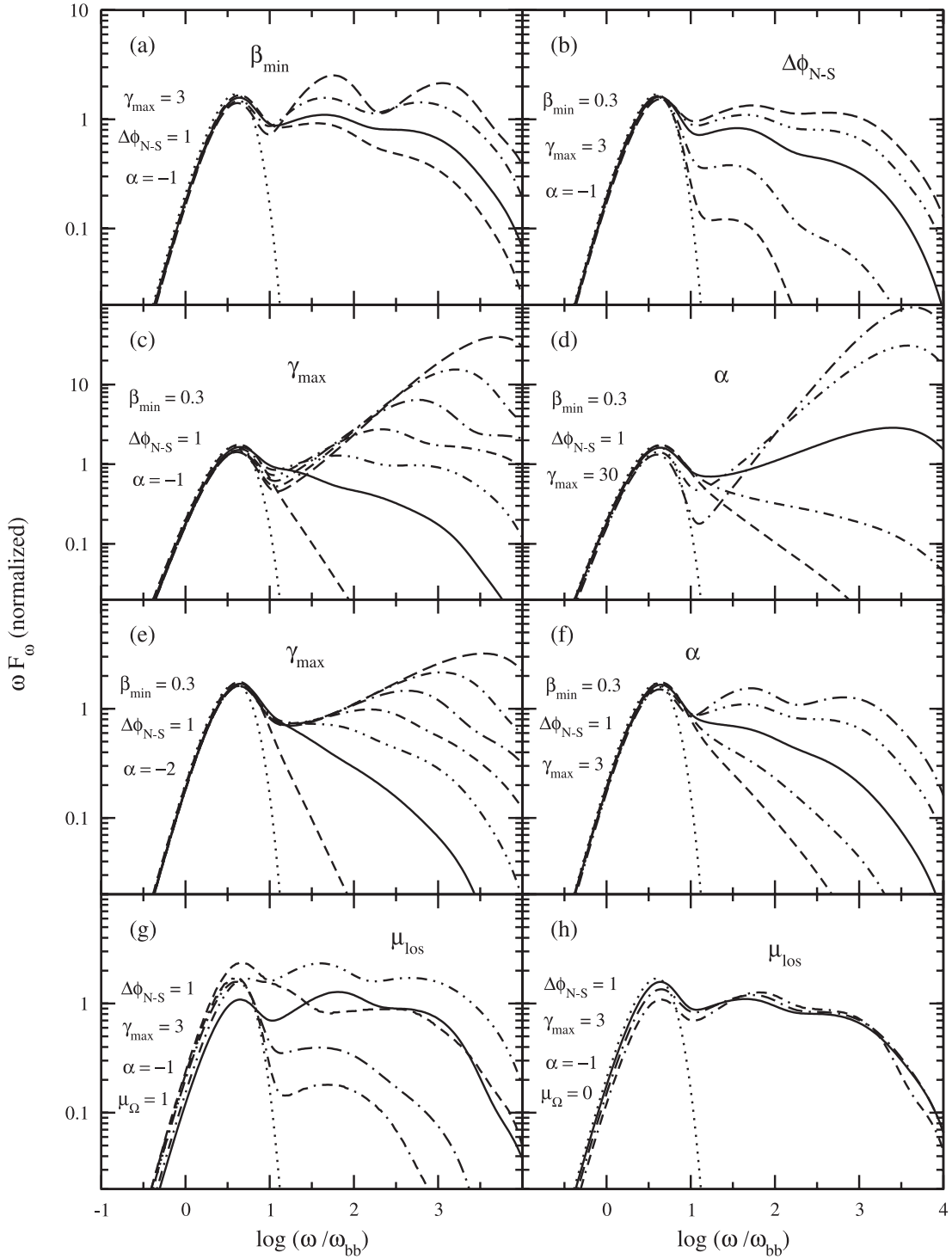
FIG. 6.—Energy spectra obtained with the broad momentum distribution, eq. (21). Normalization and frequency units are the same as Fig. 4. Panel (*a*) shows results obtained with different β_{min}, for $\gamma_{max} = 3$, $\alpha = 1$, $\Delta\phi_{N-S} = 1$, and an orthogonal configuration, $\mu_\Omega = \mu_{los} = 0$. Curves correspond to $\beta_{min} = 0.1$ (*short-dashed curve*), 0.3 (*solid curve*), 0.7 (*dot-dashed curve*), and 0.9 (*long-dashed curve*). Panel (*b*) shows the result of varying the twist angle $\Delta\phi_{N-S}$, for $\beta_{min} = 0.3$, $\gamma_{max} = 30$, $\alpha = -1$, and the same orthogonal configuration as (*a*). Curves correspond to $\Delta\phi_{N-S} = 0.1$ (*short-dashed curve*), 0.3 (*dot-dashed curve*), 0.7 (*solid curve*), 1 (*dot-dot-dashed curve*), and 1.3 (*long-dashed curve*). Panel (*c*) shows the result of varying γ_{max}, for $\beta_{min} = 0.3$ and other parameters identical to (*a*). Curves correspond to $\gamma_{max} = 1.1$ (*short-dashed curve*), 1.96 (*solid curve*), 3.48 (*dot-dot-dashed curve*), 6.19 (*dash-dash-dotted curve*), 11 (*dot–long-dashed curve*), 19.6 (*dot–short-dashed curve*), and 34.8 (*long-dashed curve*). This calculation is repeated in panel (*e*) for a softer particle distribution with index $\alpha = -2$. Panel (*d*) shows results obtained by varying the exponent α in the distribution function, for $\gamma_{max} = 30$ with the other parameters the same as in (*c*). Curves correspond to $\alpha = -4$ (*short-dashed curve*), -3 (*dot–short-dashed curve*), -2 (*solid curve*), -1 (*dot-dot-dashed curve*), and 0 (*dot–long-dashed curve*). This calculation is repeated in panel (*f*) for $\gamma_{max} = 3$. Finally, panels (*g*) and (*h*) show the aligned and orthogonal rotator configurations, respectively, analogous to those in Fig. 4*c*–4*f*, but with simulation parameters $\beta_{min} = 0.3$, $\gamma_{max} = 3$, $\alpha = -1$, and $\Delta\phi_{N-S} = 1$.

FERNÁNDEZ & THOMPSON

TABLE 1
SPECTRAL FIT PARAMETERS AND PULSED FRACTIONS FOR TYPE I VELOCITY DISTRIBUTION (BOLTZMANN, UNIDIRECTIONAL)

							PULSED FRACTION				
β_0	$\Delta\phi_{N\text{-}S}$	μ_Ω	μ_{los}	Γ	f_{pl}/f_{uns} [a]	$\omega_{bb}^{fit}/\omega_{bb}^{sim}$	I (%)	II (%)	III (%)	IV (%)	V (%)
0.2	1	0	0	7.6[b]	...	0.96	43	46	52	76	46
0.3	1	0	0	5.5[b]	...	0.92	40	45	57	81	47
0.4	1	0	0	4.3	...	0.88	41	48	64	81	50
0.5	1	0	0	3.5	23	0.90	42	49	67	83	52
0.6	1	0	0	2.9	8.2	0.92	42	48	72	83	52
0.7	1	0	0	2.4	3.9	0.94	42	47	75	86	51
0.8	1	0	0	2.0	2.0	0.95	43	46	80	91	50
0.75	0.1	0	0	2.7	0.3	0.99	15	18	64	92	23
	0.3	0	0	2.5	0.9	0.98	30	37	78	89	44
	0.7	0	0	2.3	2.1	0.96	40	46	78	88	53
	1.0	0	0	2.2	2.8	0.95	42	47	77	89	51
	1.3	0	0	2.2	3.3	0.94	43	44	78	89	49
0.6	1	1	1	3.5	1.2	0.96	0	0	0	0	0
	1	1	$1/\sqrt{2}$	3.4[b]	10	0.88	0	0	0	0	0
	1	1	0	3.1[b]	22	0.89	0	0	0	0	0
	1	1	$-1/\sqrt{2}$	2.6	...	0.86	0	0	0	0	0
	1	1	-1	3.0	8.9	0.94	0	0	0	0	0
	1	$1/\sqrt{2}$	$1/\sqrt{2}$	3.2[b]	6.0	0.92	35	27	41	50	19
	1	$1/\sqrt{2}$	0	2.9	22	0.88	10	27	59	71	39
	1	0	1	3.1	20	0.90	0	0	0	0	0
0.75	1	1	1	2.6[b]	0.5	0.97	0	0	0	0	0
	1	1	$1/\sqrt{2}$	2.6	2.3	0.92	0	0	0	0	0
	1	1	0	2.3	4.6	0.93	0	0	0	0	0
	1	1	$-1/\sqrt{2}$	2.0	7.9	0.92	0	0	0	0	0
	1	1	-1	2.5	4.6	0.95	0	0	0	0	0
	1	$1/\sqrt{2}$	$1/\sqrt{2}$	2.5	2.1	0.94	37	25	46	66	13
	1	$1/\sqrt{2}$	0	2.2	4.2	0.93	13	27	64	79	43
	1	0	1	2.3	4.5	0.93	0	0	0	0	0

[a] Entries with no data mean that setting $f_{uns} = 0$ in eq. (58) provided the best fit.
[b] Poor fit. See § 4.2 for details on the accuracy of the fitting procedure.

blackbody is present and in most cases is seen to have an approximately power-law shape.

For each output spectrum, the model described in § 4.1 was fit to the data using a Levenberg-Marquardt fitting routine (Press et al. 1992) in the frequency range $-2 < \log (\omega/\omega_{bb}^{sim}) < 1.7$. This fit involved the photon index Γ, a thermal frequency ω_{bb}^{fit} (which can differ from the input thermal frequency $\omega_{bb}^{sim} = k_B T_{bb}/\hbar$ by up to $\sim$10%), and the normalizations of the thermal (unscattered) and nonthermal (scattered) terms in equation (58). These parameters are collected in Tables 1–3 (we only tabulate the relative normalization f_{pl}/f_{uns}). In some cases, a better fit was obtained by setting $f_{uns} = 0$ in equation (58), in which case f_{pl} is an overall normalization. In general, most of the fits deviate by about 10% for $\log (\omega/\omega_{bb}^{sim}) \lesssim -1$, are accurate to a few percent in the range $-1 \lesssim \log (\omega/\omega_{bb}^{sim}) \lesssim 1$, and deviate by a varying amount (1%–100%) at higher frequencies. The label "poor fit" was added in Tables 1 and 3 when deviations from the model in the higher frequency range exceeded $\sim$50%. This is usually the case when the resonant optical depth is small.

The hardness of the high-energy spectrum correlates with twist angle, to which the optical depth is directly proportional, and with the drift velocity of the charge carriers. The dependence of the optical depth on the latter parameter is nonlinear, often coupled with geometric effects, which results in a stronger dependence of the photon index on the velocity distribution parameters than on the twist angle. A mildly relativistic Boltzmann particle distribution

function (types I–II) yields photon indices ranging from $\Gamma = 2$ (for $\beta_0 = 0.8$) to $\Gamma \gtrsim 7$ (for $\beta_0 = 0.2$ and asymmetric/symmetric particle flows along $\boldsymbol{B}$). Reducing the twist from $\Delta\phi_{N\text{-}S} = 1$ results in softer spectra. The choice of a broad relativistic distribution (III) produces approximately flat energy spectra above the blackbody peak for particle index $\alpha = -1$ and $\gamma_{max} = 3$ and for $\alpha = -2$ and a broader range of γ_{max}. Even harder spectra can be obtained by increasing the mean drift speed of the charges, but significant deviations from a power law appear in the high-energy tail.

A more distinct high-energy component of the spectrum is created when the charges have a broad, relativistic distribution of momenta (Fig. 6). The energy spectrum dips above the thermal peak and then rises as a power law up to a maximum frequency $\gamma_{max}^2 \omega_{peak}$. The photon index above the dip can be related directly to the index α of the particle distribution by assuming that each high-energy photon has scattered only once. The number flux of photons upscattered to a frequency $\gamma^2 \omega_{peak}$ is $(1/\hbar)F_\omega \propto \gamma f \propto \gamma^{1+\alpha} \propto \omega^{(1+\alpha)/2}$. The high-energy photon index is therefore

$$\Gamma = \frac{1 - \alpha}{2}. \tag{59}$$

A flat particle number distribution ($\alpha = -1$) results in a rising energy spectrum, $\omega F_\omega \propto \omega$; whereas a flat energy distribution ($\alpha = -2$) results in an energy spectrum that is somewhat softer, $\omega F_\omega \propto \omega^{1/2}$.

TABLE 2
Spectral Fit Parameters and Pulsed Fractions for Type II Velocity Distribution (Boltzmann, Bidirectional)

β_0	$\Delta\phi_{\text{N-S}}$	μ_Ω	μ_{los}	Γ	$f_{\text{pl}}/f_{\text{uns}}$ [a]	$\omega_{\text{bb}}^{\text{fit}}/\omega_{\text{bb}}^{\text{sim}}$	PULSED FRACTION				
							I (%)	II (%)	III (%)	IV (%)	V (%)
0.2	1	0	0	7.7[b]	...	0.99	35	28	12	33	27
0.3	1	0	0	5.6[b]	...	0.95	35	28	8	19	25
0.4	1	0	0	4.3[b]	...	0.91	37	28	5	16	24
0.5	1	0	0	3.6	...	0.87	39	30	7	20	24
0.6	1	0	0	3.0	11	0.92	40	32	11	24	24
0.7	1	0	0	2.5	4.8	0.94	42	34	16	30	24
0.8	1	0	0	2.1	2.4	0.96	44	36	20	40	24
0.75	0.1	0	0	2.7	0.3	0.99	15	16	33	44	18
	0.3	0	0	2.5	0.9	0.98	30	32	38	36	33
	0.7	0	0	2.4	2.4	0.96	40	37	25	22	32
	1.0	0	0	2.3	3.4	0.95	43	34	18	34	24
	1.3	0	0	2.2	4.2	0.95	45	30	27	44	14
0.6	1	1	1	3.3	4.9	0.96	0	0	0	0	0
	1	1	$1/\sqrt{2}$	2.9	...	0.84	0	0	0	0	0
	1	1	0	3.0	...	0.85	0	0	0	0	0
	1	$1/\sqrt{2}$	$1/\sqrt{2}$	3.0	14	0.92	40	31	11	20	24
	1	$1/\sqrt{2}$	0	2.9	...	0.84	6	6	9	11	7
	1	0	1	3.0	...	0.85	0	0	0	0	0
0.75	1	1	1	2.6	2.6	0.97	0	0	0	0	0
	1	1	$1/\sqrt{2}$	2.1	4.5	0.93	0	0	0	0	0
	1	1	0	2.3	5.8	0.93	0	0	0	0	0
	1	$1/\sqrt{2}$	$1/\sqrt{2}$	2.3	3.8	0.95	43	34	18	32	24
	1	$1/\sqrt{2}$	0	2.2	5.3	0.93	13	12	16	15	14
	1	0	1	2.3	5.8	0.93	0	0	0	0	0

[a] Entries with no data mean that setting $f_{\text{uns}} = 0$ in eq. (58) provided the best fit.
[b] Poor fit. See § 4.2 for details on the accuracy of the fitting procedure.

Geometric effects also strongly influence the spectrum that the observer sees. The highly anisotropic character of the emission pattern can be appreciated by comparing the spectra of the aligned rotator ($\mu_\Omega = 1$: Figs. 4c, 4e, 5c, 5e, and 6g) with those of the orthogonal rotator ($\mu_\Omega = 0$: Figs. 4d, 4f, 5d, 5f, and 6h). Changes in the observer's orientation (the value of μ_{los}) manifest themselves through variations in the relative flux of the nonthermal component and also through changes of the order of $\Delta\Gamma \sim 1$ in the photon index. Except for the nearly aligned rotator, the differences in spectral hardness resulting from a change in the observer's orientation are smaller than those that divide the spectrum of a quiescent AXP from the spectrum of an SGR.

4.3. Pulse Profiles and Pulsed Fractions

The persistent emission of the SGRs and AXPs is pulsed. The pulse profiles generally have one or two main pulses in the 1–10 keV band, but range from simple sinusoids to more complex, multipeaked profiles. The pulsed fraction, defined as

$$\text{PF} = \frac{F_{\text{max}} - F_{\text{min}}}{F_{\text{max}} + F_{\text{min}}}, \qquad (60)$$

where F_{min} and F_{max} are the minimum and maximum fluxes measured within one rotation period, ranges from a few percent to as high as ~70% (Woods & Thompson 2006). A complex pulse profile is seen more frequently in the persistent emission of the SGRs.

The pulse profiles resulting from particle velocity distributions of types I–III are displayed in Figures 7–9. (These figures corre-

spond to the spectra in Figs. 4–6.) The profiles are plotted in five frequency bands, which are taken to be

$$\begin{cases} \text{I,} & \omega/\omega_{\text{peak}} \leq 1, \\ \text{II,} & 1 \leq \omega/\omega_{\text{peak}} \leq 3, \\ \text{III,} & 3 \leq \omega/\omega_{\text{peak}} \leq 10, \\ \text{IV,} & \omega/\omega_{\text{peak}} \geq 10, \\ \text{V,} & 1 \leq \omega/\omega_{\text{peak}} \leq 10, \end{cases} \qquad (61)$$

where ω_{peak} is defined in equation (49). Each pulse profile is normalized by the pulse-averaged flux in that band; averaging over the rotation gives unit flux. The pulsed fractions are listed band by band in Tables 1–3; the values are generally accurate to 1%.

The pulse profiles have a wide variety of morphologies, and sometimes vary significantly with frequency. Several properties can be understood from the fact that the direction of a scattered photon is collimated more tightly about the direction of the magnetic field as the speed of the scattering charge increases. The differential cross section for resonant scattering is proportional to $(1 + \mu'^2)$, where μ' is the direction cosine in the rest frame of the charge after scattering (e.g., Mészáros 1992). The probability of scattering at an angle $\mu > 0$ in the stellar frame is $P(\mu > 0) = (4 + 3\beta + \beta^3)/8$ (see § 3.5). For $\beta = 0.5$ there is a 70% probability of photons being scattered in the same direction as the charge is moving.

Several trends are apparent in Figures 7–9. The pulsed fraction increases with particle drift speed, as does the asymmetry between the main pulse and the subpulse 180° away in phase (Fig. 7a). The main pulse is emitted toward the south magnetic

TABLE 3
Spectral Fit Parameters and Pulsed Fractions for Type III Velocity Distribution (Broad, Relativistic)

| β_{min} | γ_{max} | α | $\Delta\phi_{N-S}$ | μ_Ω | μ_{los} | Γ | f_{pl}/f_{uns}[a] | $\omega_{bb}^{fit}/\omega_{bb}^{sim}$ | PULSED FRACTION | | | | |
									I (%)	II (%)	III (%)	IV (%)	V (%)
0.1	3	−1	1	0	0	2.0	1.3	0.96	39	43	79	90	48
0.3	3	−1	1	0	0	1.8	1.1	0.96	38	38	83	92	45
0.7	3	−1	1	0	0	1.5	0.6	0.96	36	34	89	94	52
0.9	3	−1	1	0	0	1.1	0.3	0.98	36	34	92	96	54
0.3	1.1	−1	1	0	0	4.0[b]	...	0.83	34	39	40	45	38
	1.96	−1	1	0	0	2.3	2.4	0.93	38	39	75	81	42
	3.48	−1	1	0	0	1.7	0.9	0.97	38	37	84	94	45
	6.19	−1	1	0	0	1.5	0.5	0.98	38	36	85	97	43
	11	−1	1	0	0	1.4	0.4	0.98	38	36	84	98	39
	19.6	−1	1	0	0	1.4	0.3	0.99	38	36	83	99	35
	34.8	−1	1	0	0	1.4	0.2	0.99	38	36	81	100	32
	3	−4	1	0	0	3.3[b]	8.9	0.90	36	41	55	69	42
	3	−3	1	0	0	2.8[b]	4.2	0.92	37	41	63	78	42
	3	−2	1	0	0	2.3	2.0	0.95	38	40	74	86	42
	3	0	1	0	0	1.5	0.7	0.97	37	35	87	94	50
	3	−1	0.1	0	0	2.1	0.1	1.00	6	9	73	95	18
	3	−1	0.3	0	0	2.0	0.4	0.99	15	22	83	93	37
	3	−1	0.7	0	0	1.9	0.9	0.97	30	35	82	91	44
	3	−1	1.3	0	0	1.8	1.2	0.95	43	37	84	92	46
	3	−1	1	1	1	2.4[b]	0.3	0.96	0	0	0	0	0
	3	−1	1	1	$1/\sqrt{2}$	2.0	0.5	0.95	0	0	0	0	0
	3	−1	1	1	0	1.6	1.0	0.96	0	0	0	0	0
	3	−1	1	1	$-1/\sqrt{2}$	1.7	2.4	0.95	0	0	0	0	0
	3	−1	1	1	−1	2.3	3.5	0.94	0	0	0	0	0
	3	−1	1	$1/\sqrt{2}$	$1/\sqrt{2}$	1.8	0.5	0.96	29	17	61	82	9
	3	−1	1	$1/\sqrt{2}$	0	1.7	1.1	0.96	28	23	65	80	38
	3	−1	1	0	1	1.6	1.0	0.96	0	0	0	0	0

[a] Entries with no data mean that setting $f_{uns} = 0$ in eq. (58) provided the best fit.
[b] Poor fit. See § 4.2 for details on the accuracy of the fitting procedure.

pole, and the subpulse toward the north magnetic pole. Although the scattering particles flow out of the north pole and into the south pole, the scattering depth is largest near the magnetic equator, where the particles flow southward. The asymmetry between the main pulse and the subpulse also grows with increasing twist because of the growing asymmetry in the photon flux near the magnetic equator due to the increased optical depth there (Fig. 7b). At the same time, the main pulse divides into two subpulses, because the density of charge carriers vanishes along the magnetic axis. The subpulse is generally more distinct in the bands near the peak of the input thermal spectrum, because these photons are less scattered than those at higher energies (Figs. 7c and 7e). Finally, the pulsed fraction is generally larger for nearly orthogonal rotators (Figs. 7d and 7f).

In spite of this diversity, the axisymmetry of the magnetic field translates into a reflection symmetry of the pulse profile about phase $\phi_\Omega = \pi$. The absence of such a mirror symmetry is a direct signature of some nonaxisymmetric structure in the surface heat flux or in the magnetospheric currents, which is not accounted for in the present study.

The pulse profile also provides information about the composition of the magnetospheric corona. Some of the trends in Figure 7 are preserved when the velocity distribution is of type II (symmetric under $\beta \to -\beta$), but some differences emerge. Figure 8 displays the resulting pulse profiles; all other parameters are held constant from Figure 7. When the magnetic axis is nearly orthogonal to the rotation axis (as in Figs. 8a, 8b, 8c, and 8e), the observer must see two comparable pulses, because the charges

stream in both directions along the magnetic field. For an orthogonal rotator, as displayed here, the light curve between rotational phase 180° and 360° is, in fact, a mirror image of the light curve between 0° and 180°, but this orientation is a special case. More generally, it is possible for the observer to see a single pulse, as demonstrated in Figures 8d and 8f in the case where $\mu_\Omega = 1/\sqrt{2}$.

A single pulse can divide into two subpulses for the same reason as in Figure 7, the current density and scattering rate decrease toward the magnetic axis. One interesting feature of Figure 8 is that the positions of the subpulses can alternate by $\pi/2$ in phase between different bands; this reflects the number of scatterings that a photon in each band has typically experienced.

It should be emphasized that, aside from the number of major subpulses, which depends directly on the composition of the magnetospheric plasma, most properties of the pulse profiles depend even more strongly on orientation. A good example is provided by Figure 7f, which shows how a single-peaked profile with subpulses (dotted curve) can be transformed into a profile without any subpulse (dashed curve) and then to a double-peaked profile (solid curve) merely by changing μ_Ω and μ_{los}.

The calculated pulsed fractions P range from 0% to nearly 100%. The magnitude of P and its dependence on the simulation parameters can be quite different in the low-energy and high-energy bands. In general, the pulsed fraction correlates positively with twist angle as long as $\Delta\phi_{N-S} \lesssim 1$. The largest pulsed fractions are obtained for the broad velocity distribution (eq. [21]), as is shown in Figure 9.
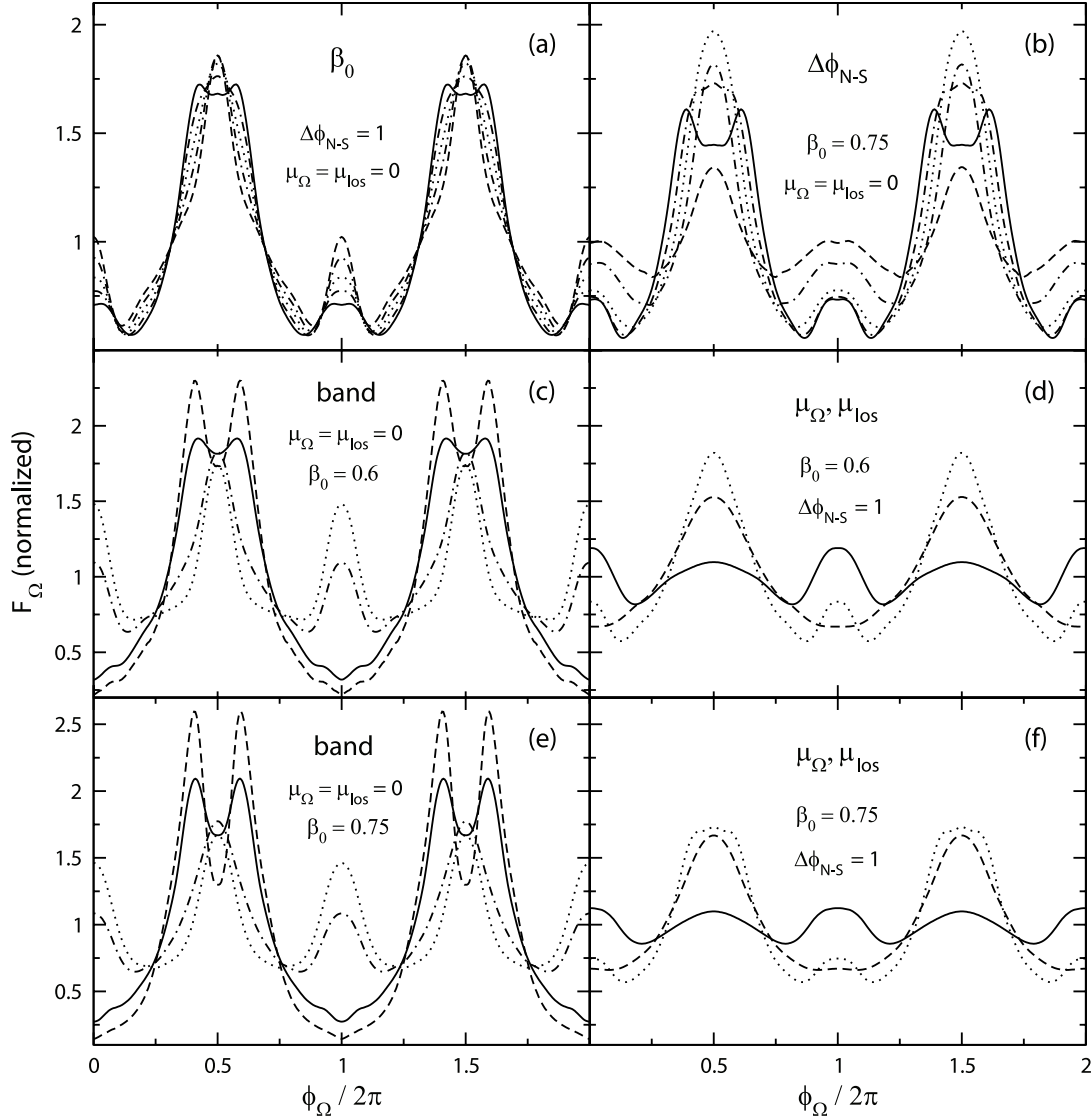
Fig. 7.—Pulse profiles obtained with a unidirectional Boltzmann particle distribution (type I; eq. [19]). All curves are normalized so that the average amplitude is unity. Simulation parameters of (a), (b), (c)–(d), and (e)–(f) are the same as in the corresponding panels in Fig. 4. Energy bands are defined in eq. (61). Curves in panel (a) show the band V profile for different velocity spreads, $\beta_0 = 0.4$ (dashed curve), 0.5 (dot-dashed curve), 0.6 (dotted curve), 0.7 (dash-dash-dotted curve), and 0.8 (solid curve). Band V pulse profiles in panel (b) correspond to different twist angles: $\Delta\phi_{N-S} = 0.1$ (dashed curve), 0.3 (dot-dashed curve), 0.7 (dotted curve), 1 (dash-dash-dotted curve), and 1.3 (solid curve). Curves in panels (c) and (e) are for different bands: I (dotted curves), II (dot-dashed curves), III (solid curves), and IV (dashed curves), with $\beta_0 = 0.6$ and 0.75, respectively. Band V pulse profiles in panels (d) and (f) correspond to different orientations of the magnetic axis and the line of sight with respect to the spin axis, $(\mu_\Omega, \mu_{los}) = (1/\sqrt{2}, 1/\sqrt{2})$ (solid curves), $(1/\sqrt{2}, 0)$ (dashed curves), and $(0, 0)$ (dotted curves), with $\beta_0 = 0.6$ and 0.75, respectively. Pulsed fractions in bands I–V for all configurations are listed in Table 1.

It should be kept in mind that the heat flux is expected to vary strongly over the surface if the elastic deformations of the crust are localized in a small area; the small radiative areas of SGR and AXP afterglows (about 1% of the neutron star surface area [Ibrahim et al. 2001; Woods & Thompson 2006]) provide evidence for this behavior. Our assumption of a single-temperature blackbody therefore involves a considerable simplification of reality, at least in the more transient magnetar sources. The combined effects of anisotropic emission and magnetospheric scattering are not examined here.

4.4. Spectral Features

Lyutikov & Gavriil (2006) suggest that spectral features in the seed photon frequency distribution may be smeared out as a result of multiple scattering in a magnetar magnetosphere. Here we test this effect with our three-dimensional Monte Carlo model.

Figure 10 shows energy spectra obtained with a narrow velocity distribution ($\bar{\beta} = 0.5, \Delta\beta = 0.1$) and large twist ($\Delta\phi_{N-S} = 1$). Instead of convolving the response function with a plain blackbody spectrum, we now add an emission line to the seed photon distribution. The line is centered at $\omega = 5k_B T_{bb}/\hbar$, with half-width $0.1\omega_{bb}$ and total flux equal to 1% of the integrated blackbody flux, as done by Lyutikov & Gavriil (2006). The spectra observed from both an aligned rotator and an orthogonal rotator are plotted. Even though the line strength is reduced by a factor of ~ 2 in some orientations, the line is not smeared out. The basic reasons are that (1) the optical depth is never very large along any direction; and (2) a substantial fraction (on the order of one-half) of the emitted blackbody photons must escape the magnetosphere directly without scattering, even if the magnetospheric twist is strong. The greatest amount of smearing would be expected in a geometry where a significant optical depth is maintained along the line of sight over
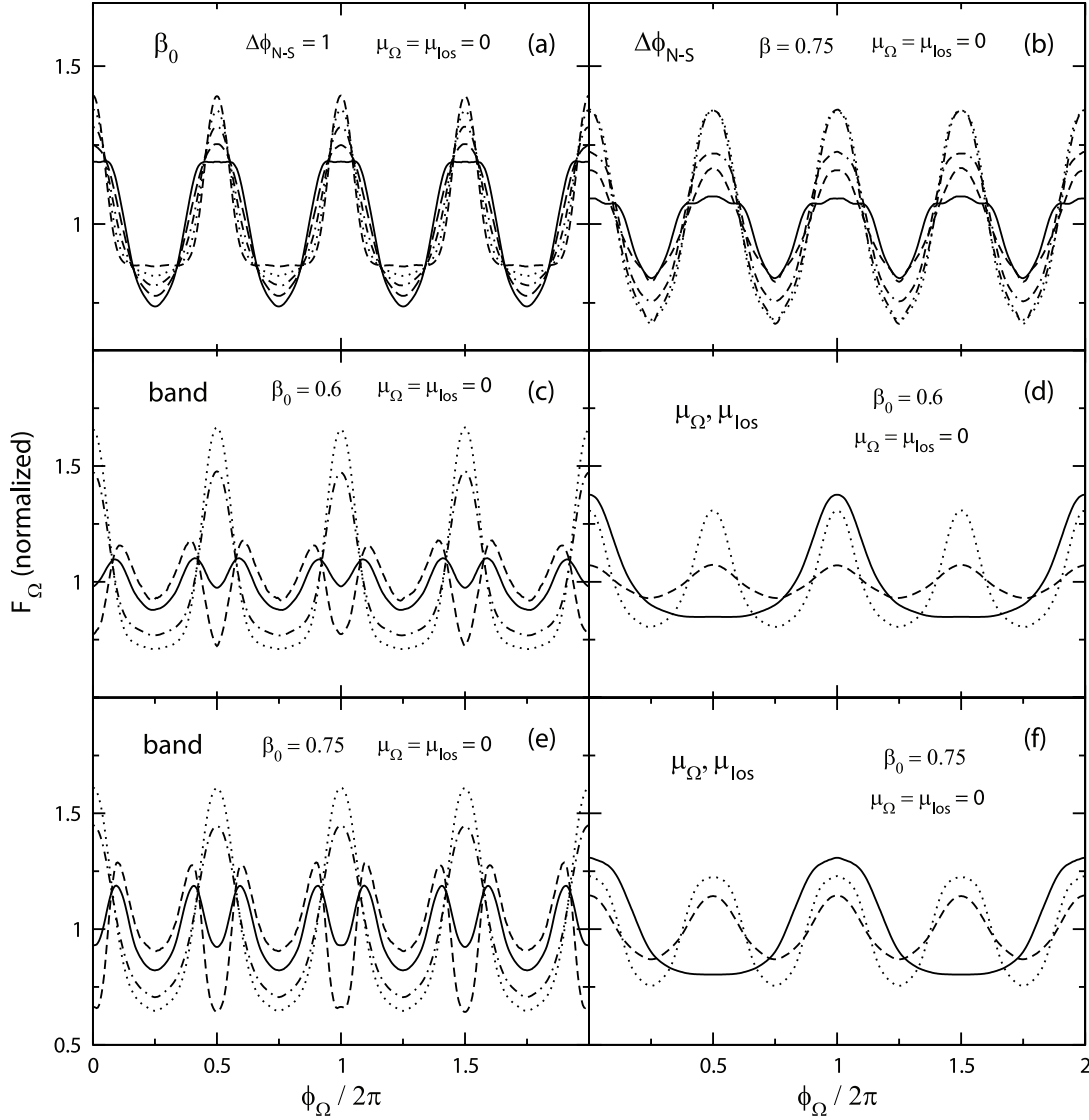
Fig. 8.—Same as Fig. 7, but for a velocity distribution function that is bidirectional, corresponding to a pair plasma (type II; eq. [19]). Simulation parameters of (*a*), (*b*), (*c*)–(*d*), and (*e*)–(*f*) are the same as those in the corresponding panels of Fig. 5. Pulsed fractions are listed in Table 2.

an entire rotation of the star. Nonetheless, a significant line feature remains even in the case of a nearly aligned rotator, with the line of sight nearly orthogonal to the magnetic and rotation axes (the lowest curve in the left panel of Fig. 10).

4.5. *Ion Scattering*

We have performed some preliminary calculations of the effects of ion cyclotron scattering on the output spectrum. We consider the case of protons (with a charge-to-mass ratio 1/1836 that of the electron). A polar magnetic field of 1×10^{15} G is chosen, which allows proton cyclotron scattering over an order-of-magnitude range in frequency above the blackbody peak.

Energy spectra and pulse profiles are shown in Figure 11. The results for protons are plotted side by side with those for electrons, using the same position-independent velocity distribution (eqs. [19]–[21]) and varying the angular distributions of the seed photons. Long-dashed curves and dot-dashed curves show results for protons assuming radial and isotropic seed photon emission, respectively, with solid and short-dashed curves containing corresponding results for electrons. The top two rows of Figure 11 assume a narrow top-hat velocity distribution. The case of a bi-

directional proton velocity distribution represents the situation in which the X-ray flux at the proton cyclotron line exceeds the Eddington flux, and a cloud of ions and electrons is blown off the stellar surface and suspended in the magnetosphere (Thompson et al. 2002). The bottom row of Figure 11 assumes a broad particle momentum distribution (type III; eq. [21]).

Multiple ion scattering generates a high-frequency power-law extension of the input thermal spectrum. The spectrum is, however, softer than that produced by electron scattering; photons that are backscattered by ions to the star can be absorbed at the stellar surface (with unit probability in the *E*-mode and with probability $\sim \frac{1}{2}$ in the *O*-mode). As expected, the high-energy spectral tail is cut off sharply at a frequency $eB_{\rm NS}/m_p c \sim (r_{\rm bb}/R_{\rm NS})^{(2+p)} \omega_{\rm peak} \sim 10 \omega_{\rm peak}$. In this calculation, the cutoff frequency for electron scattering is $m_p/m_e \sim 10^3$ times higher. We have not displayed this cutoff, because the calculation does not include the effects of electron recoil (which becomes important at 50–100 keV) or relativistic corrections to the scattering cross section at the first Landau resonance. Recoil effects can be entirely neglected for ion scattering.

The effects of ion scattering could in principle be discerned during a very luminous phase, e.g., the afterglow following an
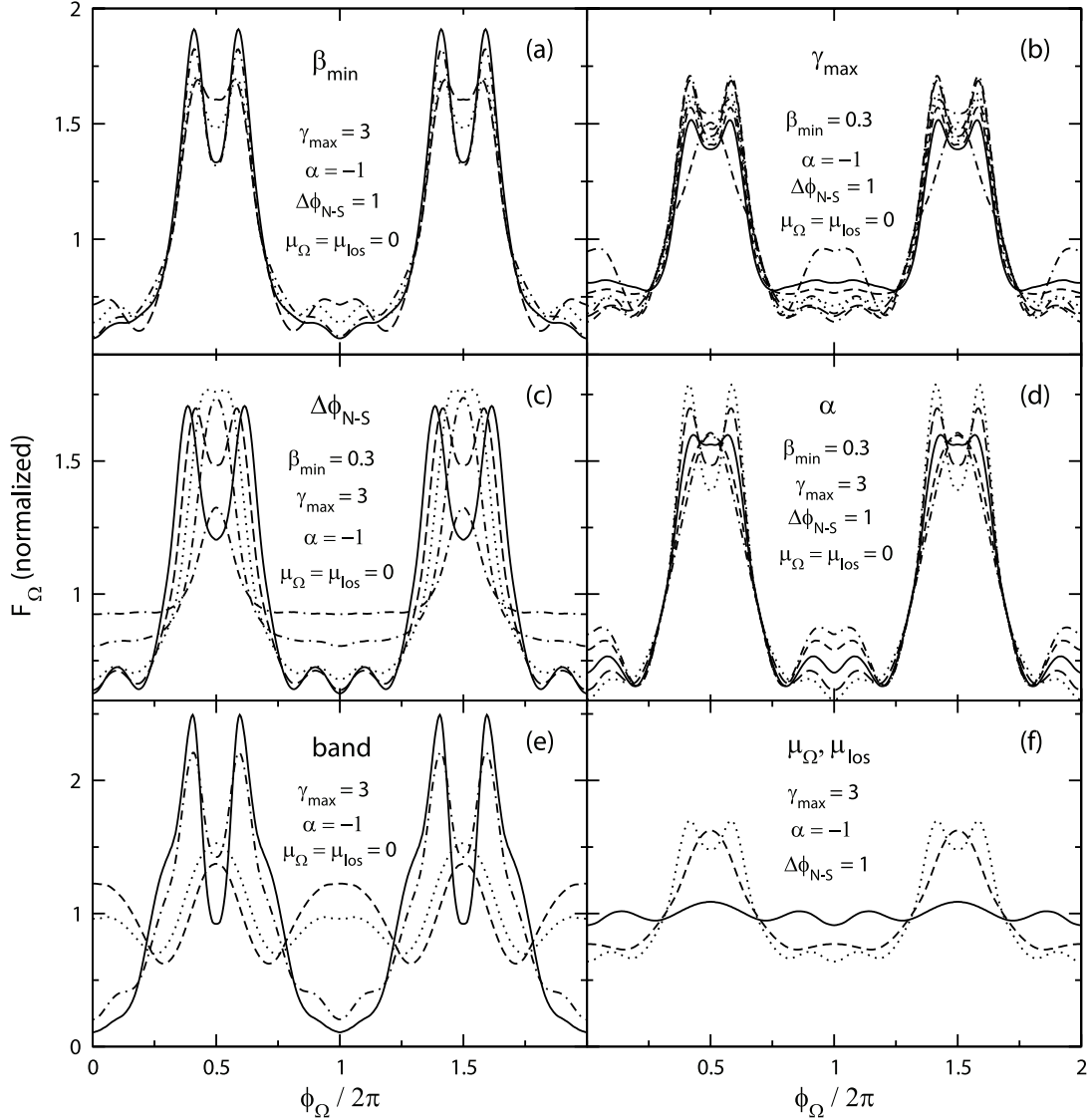
FIG. 9.—Pulse profiles obtained with the broad velocity distribution function, eq. (21), with the same normalization as Fig. 7. Simulation parameters are as shown on each panel. Panel (*a*) shows profiles in band V obtained with different minimum velocities, with curves corresponding to $\beta_{min} = 0.1$ (*dashed curve*), 0.3 (*dotted curve*), 0.7 (*dot-dashed curve*), and 0.9 (*solid curve*). Panel (*b*) shows the result of varying the maximum Lorentz factor, with curves corresponding to $\gamma_{max} = 1.1$ (*dash-dash-dotted curve*), 1.96 (*dot-dot-dashed curve*), 3.48 (*dash-dotted curve*), 6.19 (*long-dashed curve*), 11 (*dotted curve*), 19.6 (*short-dashed curve*), and 34.8 (*solid curve*). Panel (*c*) shows results for different twist angles, with curves corresponding to $\Delta\phi_{N\text{-}S} = 0.1$ (*dash-dash-dotted curve*), 0.3 (*dash-dotted curve*), 0.7 (*dotted curve*), 1 (*long-dashed curve*), and 1.3 (*solid curve*). Panel (*d*) shows the result of varying the exponent of the distribution function, with curves corresponding to $\alpha = -4$ (*dot-dashed curve*), -3 (*short-dashed curve*), -2 (*solid curve*), -1 (*long-dashed curve*), and 0 (*dotted curve*). Panel (*e*) shows light curves in bands I (*dashed curve*), II (*dotted curve*), III (*dot-dashed curve*), and IV (*solid curve*), for $\beta_{min} = 0.3$, $\gamma_{max} = 3$, $\alpha = -1$, $\Delta\phi_{N\text{-}S} = 1$, and $\mu_{\Omega} = \mu_{los} = 0$. Panel (*f*) shows profiles in band V obtained from the same simulation as (*e*), but varying the orientation as $(\mu_{\Omega}, \mu_{los}) = (1/\sqrt{2}, 1/\sqrt{2})$ (*solid curve*), $(1/\sqrt{2}, 0)$ (*dashed curve*), and $(0, 0)$ (*dotted curve*). Pulsed fractions are shown in Table 3.

intermediate-energy SGR burst. For example, the afterglow of the 29 August 1998 burst of SGR 1900+14 showed a marked spectral hardening in the 2–5 and 5–10 keV bands but not in the 10–20 keV band (Ibrahim et al. 2001).

Results for proton scattering are sensitive to the angular distribution of seed photons, given the smaller resonant radius (Fig. 11). The spectra become harder when the angular distribution is changed from radial to isotropic. By contrast, spectra obtained with electron scattering are almost independent of the input angular distribution, with results for the radial and isotropic case being hardly distinguishable.

The pulses produced by ion and electron scattering have a similar morphology (Fig. 11), although electron scattering yields smaller pulsed fractions. Again, results for protons are somewhat sensitive to the angular distribution of seed photons, while the same parameter does not influence pulse profiles obtained with

electron scattering. A proper account of ion scattering must include the effects of light bending of the photon trajectories

4.6. *Seed Photon Polarization*

There are two possible sources of seed X-ray photons: internal heating by a decaying magnetic field (e.g., Thompson & Duncan 1996; Heyl & Kulkarni 1998; Arras et al. 2004) and the bombardment of the surface by energetic charges (Thompson et al. 2002). In the first case, the seed photons are emitted in the *E*-mode if the magnetic field is stronger than $\sim 10^{14}$ G (Ho & Lai 2004). In the second case, the emission is in the *O*-mode if the charges are stopped by Coulomb collisions in a surface layer that is optically thick to free-free absorption.

It is therefore interesting to explore whether these two types of seed photons can be distinguished using the output X-ray spectrum or pulse profiles. The scattering cross sections of the two
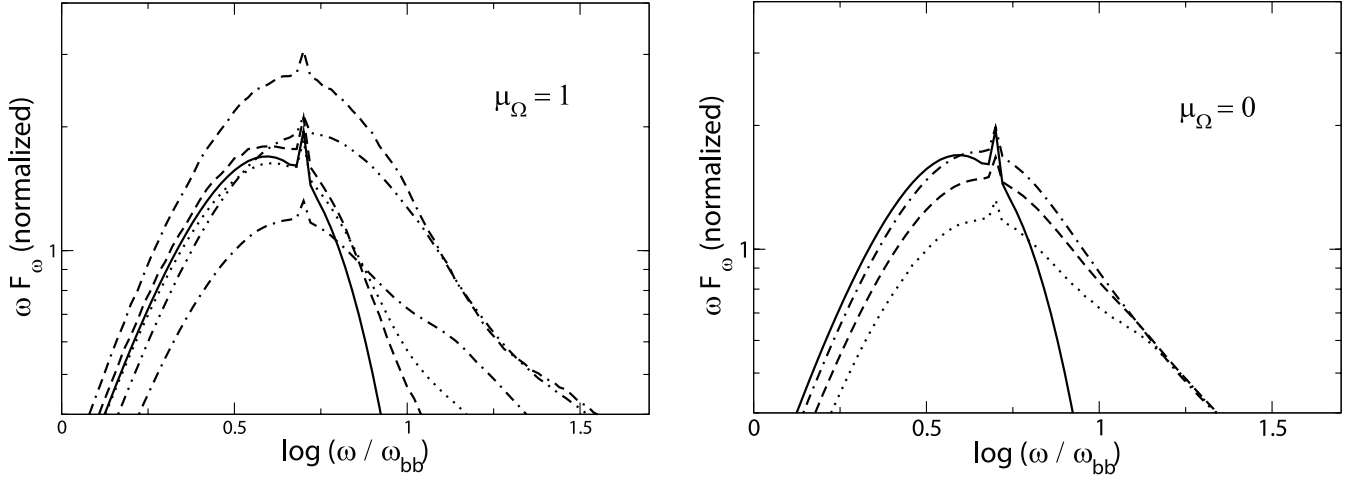
FIG. 10.—Effect of magnetospheric scattering on an emission line. Input spectra (*solid curves*) have a line centered at $\omega = 5k_{\rm B}T_{\rm bb}/\hbar$, with half-width $0.1k_{\rm B}T_{\rm bb}/\hbar$ and total energy equal to 1% of the blackbody. Output spectra are obtained by convolving the input with the magnetospheric response function for different orientations. *Left*: Aligned rotator ($\mu_\Omega = 1$), with $\mu_{\rm los} = 1$ (*dashed curve*), $1/\sqrt{2}$ (*dotted curve*), 0 (*dot-dashed curve*), $-1/\sqrt{2}$ (*dot-dot-dashed curve*), and -1 (*dash-dash-dotted curve*). *Right*: Orthogonal rotator ($\mu_\Omega = 0$), with $\mu_{\rm los} = 1$ (*dotted curve*), $1/\sqrt{2}$ (*dashed curve*), and 0 (*dot-dashed curve*). Velocity distribution is monoenergetic and unidirectional (eq. [36]), with a mean drift speed $\bar{\beta} = 0.5$ and a total width $\Delta\beta = 0.1$. The twist angle is $\Delta\phi_{\rm N-S} = 1$.
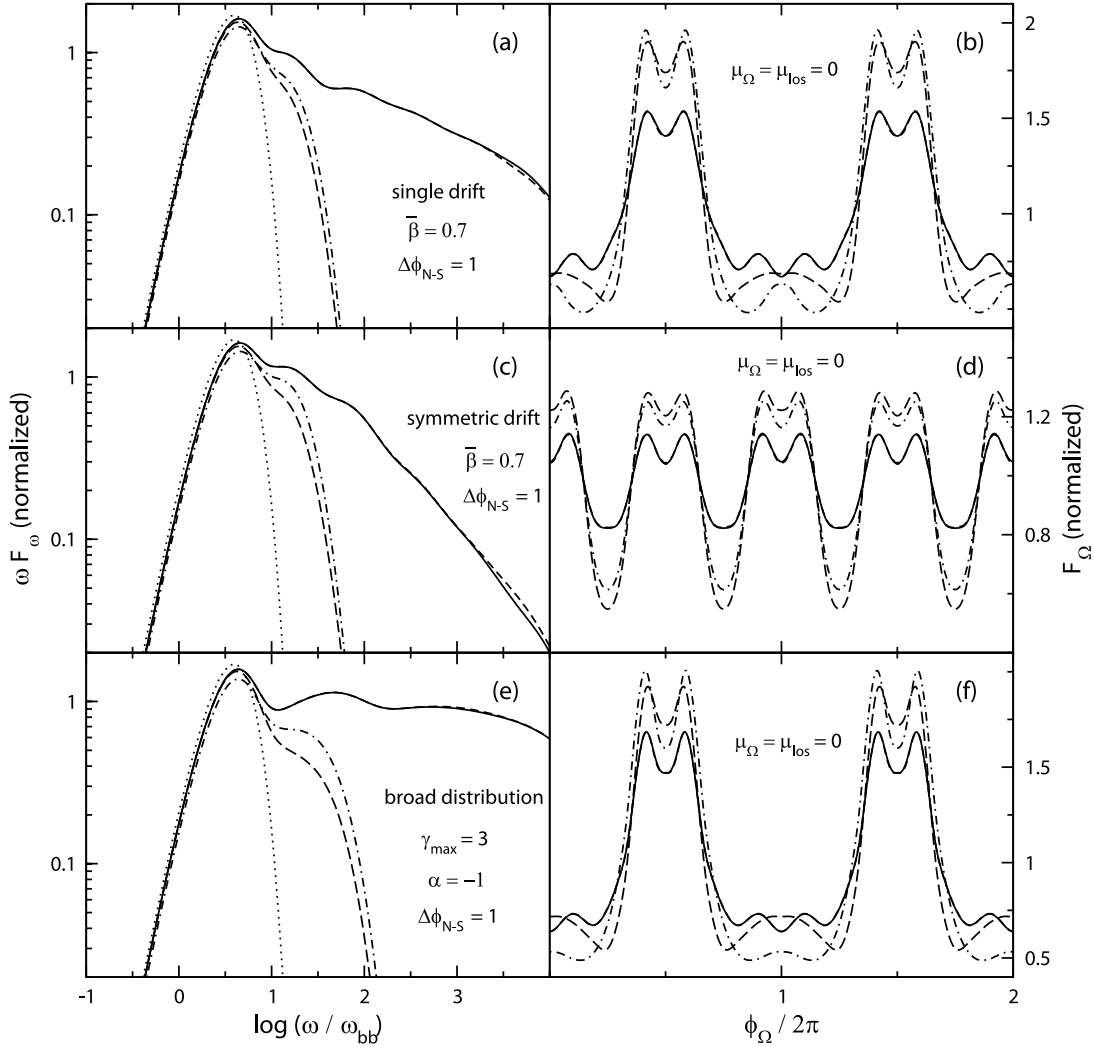
FIG. 11.—Energy spectra (*left column*) and band V pulse profiles (*right column*) obtained for $B_{\rm pole} = 10^{15}$ G and a charge/mass ratio equal to that of the proton and the electron. We allow for radial (*long-dashed curves*: proton; *solid curves*: electron) and isotropic (*dot-dashed curves*: proton; *short-dashed curves*: electron) angular distributions of the seed photons. Panels (*a*) and (*b*) are for a monoenergetic, unidirectional particle distribution (eq. [36]) with mean drift $\bar{\beta} = 0.7$ and $\Delta\beta = 0.1$. In panels (*c*) and (*d*), the velocity distribution is monoenergetic and bidirectional, as is appropriate to the case in which the ions are driven off the surface of the magnetar by radiation pressure. Other parameters are the same. In panels (*e*) and (*f*), the velocity distribution is broad and relativistic (type III; eq. [21]), with $\beta_{\rm min} = 0.3$, $\gamma_{\rm max} = 3$, and $\alpha = -1$. All curves assume $\Delta\phi_{\rm N-S} = 1$ and $\mu_\Omega = \mu_{\rm los} = 0$. Curves for electrons are almost undistinguishable.
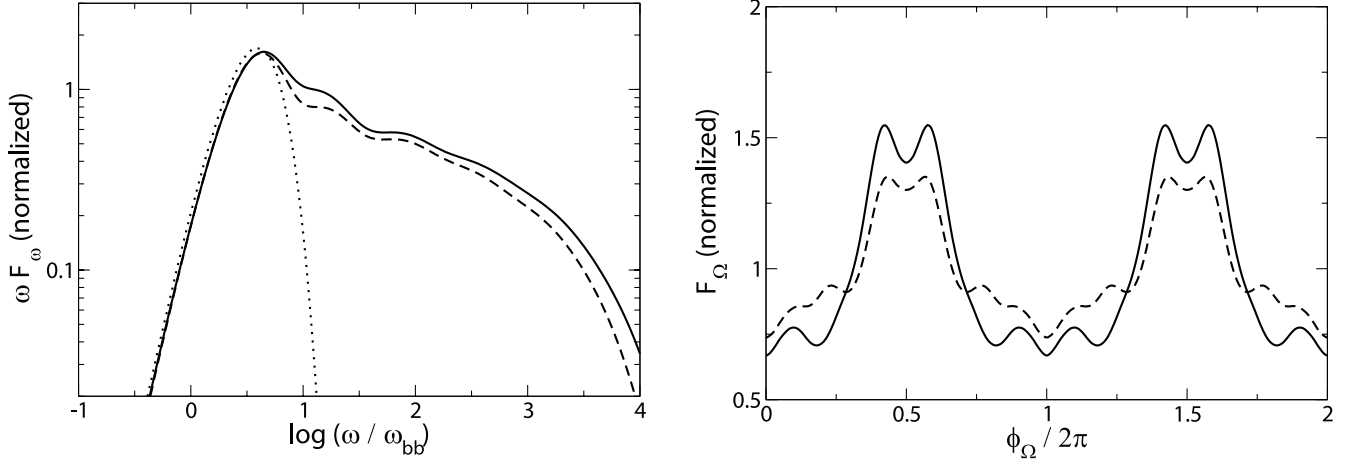
Fig. 12.—Energy spectra (*left*) and band V pulse profile (*right*) corresponding to 100% polarization of the seed photons in the *E*-mode (*solid curves*) and the *O*-mode (*dashed curves*). The velocity distribution is monoenergetic and unidirectional (eq. [36]) with mean drift speed $\bar{\beta} = 0.7$ and total width $\Delta\beta = 0.1$. In addition, $\Delta\phi_{\text{N-S}} = 1$ and $\mu_\Omega = \mu_{\text{los}} = 0$.

modes at the cyclotron resonance are comparable, because the electromagnetic eigenmodes are determined by vacuum polarization effects and are linearly polarized even in the core of the cyclotron resonance (§ 2). For this reason, one expects similar pulse profiles and nonthermal spectra for both polarizations of the seed photons. Nonetheless, the scattering cross section of an *O*-mode photon is suppressed with respect to that of an *E*-mode photon by a factor $(\mu')^2$ (eqs. [13] and [15]; see also the discussion in Appendix A). One therefore expects the spectra to be slightly softer and the pulsed fractions to be slightly lower when the seed photons are injected in the *O*-mode.

Figure 12 shows energy spectra (*left*) and pulse profiles in band V (*right*) using the same magnetospheric parameters, excepting that the seed photons are 100% polarized in the *E*-mode (*solid curves*) and the *O*-mode (*dashed curves*). In the second case, the nonthermal tail does indeed have a slightly lower amplitude compared with the blackbody peak, and the pulsed fraction is smaller. Nevertheless, the changes in the emission pattern resulting from the polarization of the seed photons are much subtler than those produced by changes in the orientation of the star (§§ 4.2 and 4.3), offering little chance of identifying the seed photon emission mechanism except through direct polarization measurements.

5. DISCUSSION

We have developed a Monte Carlo code to study the reprocessing of thermal X-rays by resonant cyclotron scattering in neutron star magnetospheres using the model of Thompson et al. (2002). The code is fully three dimensional and allows for an arbitrary velocity distribution of the scattering particles and an arbitrary magnetic field geometry. Angle-dependent X-ray spectra and pulse profiles can be calculated for an arbitrary orientation between the magnetic axis and the spin axis and between the spin axis and the line of sight to the star.

Our aim here has been to show which types of X-ray spectra and pulse profiles follow generically from the model and which may point to different emission mechanisms. We can reproduce most of the properties of the 1–10 keV emission of the AXPs, but not of the SGRs, by assuming a broad and mildly relativistic velocity distribution and moderate twist angles ($\Delta\phi_{\text{N-S}} \sim 0.3$–1 radian). In particular, the SGRs in their most active states have harder X-ray spectra than can be reproduced by the model (Woods et al. 2007). Our results demonstrate that changes in the strength of the twist and in the dynamics of the charged particles (which are

coupled strongly to the radiation field) can lead to substantial changes in flux, hardness, pulse shape, and pulsed fraction.

5.1. *Relative Strength of the Thermal and Nonthermal Components of the X-ray Spectrum*

The X-ray spectra of most magnetars display a prominent thermal component. The corresponding blackbody area is less than, or sometimes comparable to, the expected surface area of a neutron star (e.g., Woods & Thompson 2006). In sources where the blackbody component is dominant at ~1–3 keV, the high-energy photon index is typically 2 or softer. However, SGR 1900+14 presents an example of an SGR in which a thermal component and a hard power-law component of the spectrum are simultaneously present (Esposito et al. 2007).

Model spectra with a mildly relativistic particle distribution ($k_{\text{B}}T_0 \simeq 0.5 m_e c^2$, $\beta_0 \simeq 0.75$; eq. [19]) can easily reproduce the 1–10 keV spectra of sources like 4U 0142+614, 1RXS J170849−4009, and 1E 1841−045. Some of our model spectra show a noticeable downward break at ~30–50$k_{\text{B}}T_{\text{bb}} \simeq 10$–30 keV (e.g., Figs. 4*f* and 5*f*). Such a break may be present in the combined *XMM-Newton* and *INTEGRAL* spectra of SGR 1900+14 (Götz et al. 2006), and its presence is not excluded in other sources, such as the AXPs 4U 0142+614 and 1E 1841−045, when one takes into account the presence of a separately rising high-energy spectral component above 20 keV (Kuiper et al. 2006; Götz et al. 2006).

The quiescent SGRs have relatively weak blackbody components to their spectra, and during periods of extreme activity, a pure power-law fit to the spectrum can have a photon index of ~−1.6 (Mereghetti et al. 2005; Woods et al. 2007). (Even harder photon indices are obtained from combined blackbody + power-law fits to the spectrum, but then the continuation of the 2–10 keV fit to higher energies disagrees with the *INTEGRAL* flux measurements.) We could obtain spectra as hard as this by choosing a broad power-law momentum distribution for the magnetospheric charges (Fig. 6), but the output spectrum then displays a strong blackbody component. In the fit of Esposito et al. (2007) for SGR 1900+14, the amplitude of the blackbody component is about 3 times that of the power-law component at the blackbody peak, whereas in the spectra of Figure 6*b*, it is 6–8 times larger.

We expect this conclusion to hold for any model for the high-energy continuum that relies on the upscattering of the thermal seed photons. Balancing the energy input to the coronal charges

with the loss by upscattering, one finds that $\tau(\langle\gamma^2\rangle - 1) \sim 1$ (as in corona models based on nonmagnetic Compton scattering). When $\langle\gamma^2\rangle^{1/2} \gg 1$, it is generally not possible to upscatter a large fraction of the thermal photons, because the optical depth τ of the corona is small. The results obtained with a broad relativistic particle distribution function should also be treated with caution; the charges are subject to a strong cyclotron drag force at a radius of $\sim 50-100$ km, where the cyclotron energy is $1-10$ keV, so it is probably not self-consistent to assume that they have the same distribution function there as they do in the inner parts of the magnetosphere.

These considerations point to the conclusion that the hard non-thermal spectral states of the SGRs (with photon indices <2) have an origin that is similar to that of the *excess* high-energy emission that is observed from several AXPs above 20 keV. In the magnetar model, this high-energy emission must involve a different emission process, such as bremsstrahlung from a hot transition layer between the relativistic corona and the colder neutron star atmosphere or synchrotron emission triggered by pair cascades at a distance of ~ 100 km, where the electron cyclotron energy is ~ 1 keV (Thompson & Beloborodov 2005).

Indeed, there are reasons to expect that some active magnetars (e.g., the SGRs) can have significantly reduced X-ray emission due to deep internal cooling, even when the time-averaged rate of magnetic field decay remains high. Large increases in the neutrino emissivity are expected when the core neutrons undergo a super-fluid transition, which leads to an order-of-magnitude drop in blackbody X-ray flux (Arras et al. 2004). Given the high-absorbing columns $N_H \sim (2-6) \times 10^{22}$ cm^{-2} that are inferred from the soft X-ray spectra of the two active SGRs, it would then be possible to hide the surface thermal component from detection. (The combination of a low thermal luminosity and strong absorption does not remove the inconsistency with the model spectra in Figs. $6c-6e$; the models then would predict that the nonthermal continuum is much dimmer than $\sim 10^{35}$ ergs s^{-1} at a photon energy of a few keV.)

5.2. Low-Energy X-ray Spectra

Our results show that the rescattering of thermal photons by magnetospheric charges does not lead to any enhanced emission at energies below the peak of the seed X-ray distribution. Our new fitting formula, equation (58), takes this low-energy behavior of resonant scattering into account.

It should be kept in mind that the softest power-law components in measured spectra are typically needed to fit a *low-energy* excess to a single-temperature blackbody. In our model, most of the emission below the thermal peak comes from unscattered photons; our rotationally averaged spectra have a Rayleigh-Jeans shape at low energies, which lies just below the input blackbody distribution. We therefore suggest that a fit to an AXP X-ray spectrum involving a small N_H and a very soft power-law component is physically inconsistent, and that in such a case the fitting formula from equation (58) is strongly preferred. Of course, the softest AXP spectra can also be fitted by a superposition of two or more blackbody components (e.g., Halpern & Gotthelf 2005).

The formation of a high-energy tail in the output spectrum is closely tied, in this model, to an increased spin-down rate (due to the flaring out of the poloidal field lines as they are twisted). The AXP 1E 2259+586 provides an example of a magnetar that has demonstrated SGR-like burst activity (Woods et al. 2004), but which also has the lowest spin-down rate of any magnetar candidate, a very soft $1-10$ keV spectrum, and only an upper bound on the 100 keV emission that has been detected from several other AXPs (Kuiper et al. 2006). We would therefore expect that the

$1-10$ keV spectrum of 1E 2259+586 is most accurately modeled by a variable surface temperature, rather than by a combination of thermal and nonthermal components.

Indeed, a recent reanalysis of the X-ray spectra of several AXPs has revealed a broader spectrum than a pure single-temperature blackbody near the thermal peak (Durant & van Kerkwijk 2006b). This suggests that the thermal X-ray flux is distributed inhomogeneously across the surface of the neutron star. This is expected given the inhomogeneous nature of the yielding behavior in the crust of a magnetar and the anisotropy of the thermal conductivity in the presence of a strong magnetic field (Thompson & Duncan 1996; Lyubarsky et al. 2002; Pérez-Azorín et al. 2006; Geppert et al. 2006).

5.3. Pulse Profiles and Pulsed Fractions

Our calculations generally reproduce X-ray pulse profiles that are characteristic of the AXPs: single or multiple peaks, with sinusoidal shapes and sometimes the presence of narrow subpulses. The strong angular dependence of the optical depth to resonant scattering explains why phase-resolved spectra show variations in both their flux level and hardness (e.g., Tiengo et al. 2005; Göhler et al. 2005). We find that the X-ray spectrum is generally hardest at pulse maximum, in agreement with some measurements (Mereghetti et al. 2004; Tiengo et al. 2005).

The number of subpulses depends essentially on the orientation of the spin and magnetic axes of the neutron star, which are not constrained by any independent measurements. The pulse profiles of the actively bursting SGRs tend to be more complicated, which may reflect the presence of high-order multipoles in the current flowing near the stellar surface. As discussed in § 5.1, their very hard X-ray spectra are more consistent with a separate emission process, possibly localized close to the surface of the neutron star.

Pulsed fractions as high as $\sim 40-50\%$ near the blackbody peak are easily obtained from the anisotropic scattering of thermal photons in the magnetosphere (Tables 1–3). Significantly higher pulsed fractions are possible in the power-law tail of the spectrum due to the increased anisotropy of the multiply scattered photons. It should be emphasized that this result is obtained assuming a *spherically symmetric* source of seed photons, i.e., a constant temperature across the surface of the neutron star. Only in one object (the AXP 1E 1048.1$-$5957) is the pulsed fraction significantly higher (70%$-$80%) in the $1-10$ keV range (Tiengo et al. 2005). It should be possible to obtain higher pulsed fractions if the seed photons are emitted at localized hotspots, as suggested by the small blackbody emitting area (Durant & van Kerkwijk 2006a). Our calculations are therefore complementary to those of Psaltis et al. (2000), Özel et al. (2001), and Özel (2002), who studied the pulse profiles and pulsed fractions that result from isolated hotspots on rotating neutron stars and compared their calculations with the observed $1-10$ keV pulse profiles of the AXPs.

5.4. Comparison with Previous Work

Semianalytical work on resonant cyclotron scattering in the atmospheres of neutron stars goes back to the 1980s, the original focus being the transfer of radiation through the atmosphere of the star or through an accretion column (Yahel 1979; Wasserman & Salpeter 1980; Nagel 1980; Mészáros & Nagel 1985a, 1985b). In these calculations, the geometrical thickness of the scattering material was generally taken to be small compared with the gradient scale of the magnetic field. The effect of magnetic field inhomogeneity was analyzed by Zheleznyakov (1996), who found solutions to the one-dimensional radiative transfer equation using the Schwarzschild-Schuster method. Lyutikov & Gavriil (2006)

generalized this method to include the combined effects of the particle motion and magnetic field inhomogeneity. In the limit of small particle dispersion βc, they found that the radiation spectrum that is transferred through an optically thick medium is up-scattered in energy by a factor $1 + 2\beta$. This model was shown to provide a good fit to the 1–10 keV spectrum of 1E 1048.1−5937, the AXP source in which the thermal component of the spectrum peaks at the highest frequency. However, this nonrelativistic and one-dimensional approximation cannot provide a realistic description of the more extended high-energy spectra that are observed in some magnetars, including the slope of the power-law tail, the relative amplitude of the power-law and thermal components, or the detailed shape and frequency dependence of the pulse profiles.

Monte Carlo codes for resonant cyclotron scattering through the surface layers of a neutron star were developed around the same time (e.g., Pravdo & Bussard 1981; Wang et al. 1988) and also applied to the problem of line formation in gamma-ray bursts (Wang et al. 1993). The last two studies remain the most realistic to date, as they include the effects of thermal broadening, vacuum and plasma polarization, and electron recoil. All these effects but the last one are included in our study (plasma makes a negligible contribution to the dielectric properties of the magnetosphere at frequencies of 10^{17}–10^{19} Hz). However, these studies are all one-dimensional and focus on the regime of very large optical depth and a weak gradient in the magnetic field, so the results cannot be compared directly with ours.

5.5. Further Developments

We now discuss how some of the key simplifications of the model will need to be relaxed in future work.

Anisotropic radiation pressure.—The most important simplification in the treatment of the transfer of radiation through the magnetosphere is the decoupling of the particle dynamics from the radiation force that is imparted through cyclotron scattering. An electric field is induced by the twisted magnetic field lines, which lifts charged particles off the stellar surface and accelerates them to high speeds (Thompson et al. 2002; Beloborodov & Thompson 2007). When the Lorentz-boosted cyclotron energy lies in the range 1–10 keV (or 1–100 keV for an active SGR), the particle moving against the direction in which the radiation is flowing feels a strong drag force, and a strong electric field is required to compensate (Thompson & Beloborodov 2005). The charged particle dynamics and the radiation transfer are therefore strongly coupled.

Particle recoil.—The noninclusion of particle recoil after scattering leads to significant errors in the shape of the output spectra above ~ 100 keV. The spectra obtained with broad relativistic particle distributions involve essentially the single scattering of photons of a frequency $\sim \omega_{\mathrm{peak}} = 2.82 k_{\mathrm{B}} T_{\mathrm{bb}}/\hbar$. Recoil is important only when $\gamma \gtrsim m_e c^2 / 2\hbar \omega_{\mathrm{peak}}$ and $\hbar\omega \sim \gamma^2 \omega_{\mathrm{peak}} \gtrsim 100$ MeV, where we do not tabulate spectra. It should be emphasized that this remains a technical issue insofar as additional emission mechanisms dominate at ~ 30–100 keV (see § 5.1).

Seed photon distribution.—In all our simulations we have assumed that the seed photons are emitted radially, from points uniformly distributed over the stellar surface, and with a single polarization. There are several reasons for this choice. First, the radius of first scattering by electrons (or positrons) is $R_{\mathrm{res}} \sim 10 R_{\mathrm{NS}}$; second, we are not including the effects of temperature inhomogeneities on the neutron star surface, focusing instead on the pulsations that result from the transport of X-ray photons through a twisted magnetosphere. The effects of light bending must be included as soon as this second assumption is relaxed.

Polarization.—Continuum spectra and pulse profiles do not provide a clear way of discriminating between thermal emission from the surface due to deep cooling (*E*-mode emission) and due to particle bombardment and stopping by Coulomb collisions (*O*-mode emission). In both cases, the surface temperature will in practice be anisotropic (due to the channeling of the cooling heat flux along the magnetic field and due to variations in the strength of the twist across the surface). In the second case, one expects the intensity of the *O*-mode photons to be more strongly beamed along the local direction of the surface magnetic field (e.g., Basko & Sunyaev 1975), but we have found that pulsed fractions of 40%–50% percent are achievable solely by radiation transport through the magnetosphere. Polarization measurements of AXPs and SGRs would say much about the physics of the beam-heated atmosphere of a magnetar and the distribution of magnetospheric currents, but they require polarimeters that are sensitive at flux levels of $\sim 10^{-11}$ ergs cm^{-2} s^{-1} in the 1–10 keV band.

Magnetic field geometry.—The magnetospheric model employed by Thompson et al. (2002) is self-similar; the pitch angle of the external field lines is independent of distance from the neutron star. Clearly different X-ray spectra and pulse profiles will result if the current is distributed in a different way throughout the magnetosphere. Observations that show a delayed increase in the spin-down torque following periods of X-ray burst activity (Woods et al. 2002) suggest that the twist is not distributed homogeneously throughout the magnetosphere in the immediate aftermath of a crustal yielding event. Quadrupole and octopole components of the magnetic field have a large effect on the pulse profile only if ions are the dominant scattering species or if the nonthermal emission is localized close to the neutron star surface (as it is with bremsstrahlung emission; Thompson & Beloborodov 2005).

APPENDIX A

CODE TESTS

A1. INPUT FREQUENCY DISTRIBUTION AND GENERAL OUTPUT

The output spectrum resulting from the input of a monochromatic line (frequency ω_{in}) is obtained by integrating the response function R (eq. [47]) over magnetic polar angle μ_k. Well-sampled spectra and pulse profiles are obtained with 10^7 photons per run, using bins of size 0.02 in log (ω) and 0.01 in μ_k. Figure 13 (*left column*) shows the result for a monoenergetic particle distribution function (eq. [36]) with
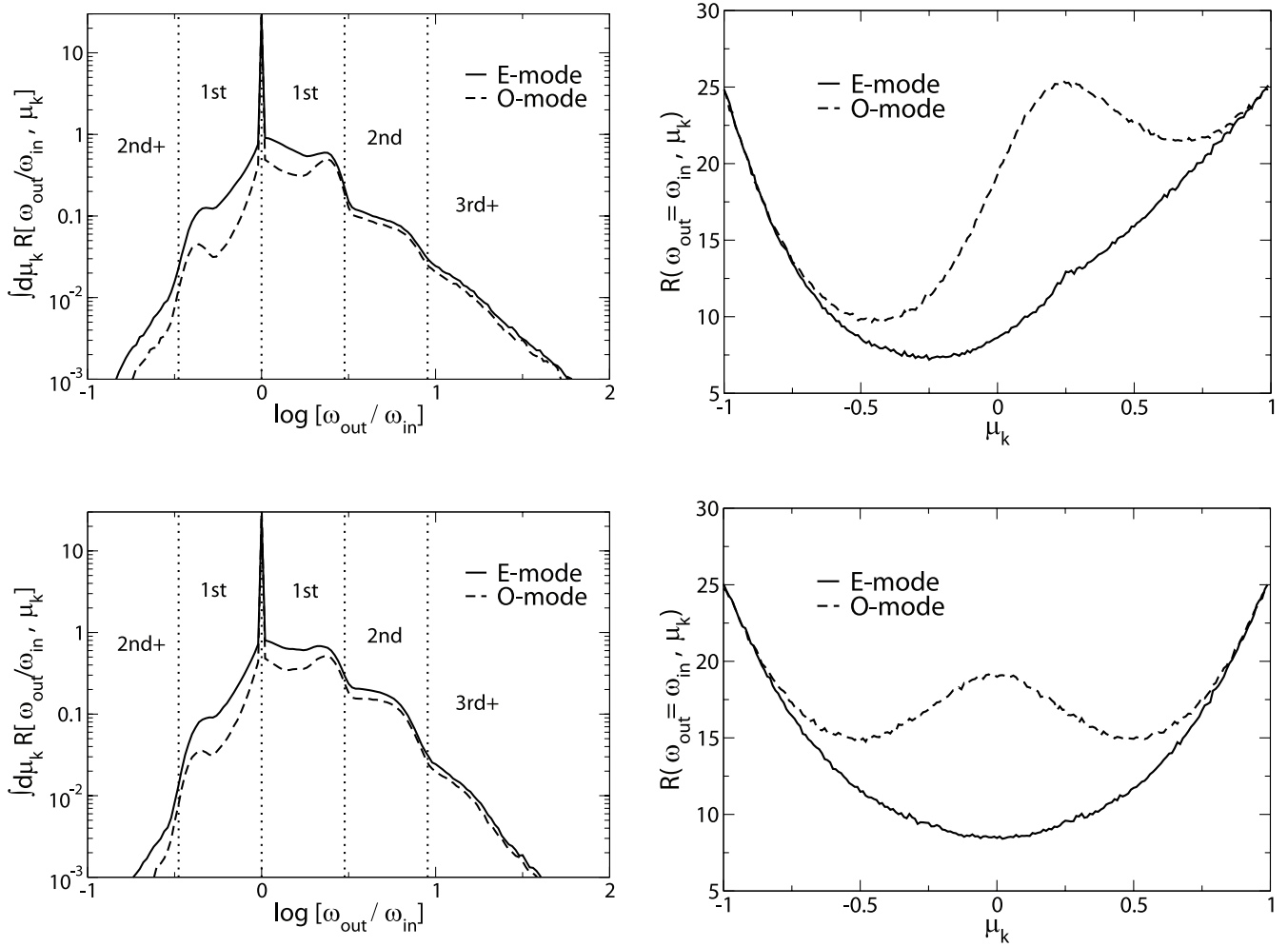
FIG. 13.—*Left*: Output spectrum in a twisted magnetosphere ($\Delta\phi_{\text{N-S}} = 1$) obtained by integrating eq. (47) over magnetic polar angle. Seed photons are injected in either the *E*-mode (*solid curves*) or the *O*-mode (*dashed curves*). Vertical dotted curves mark out the maximum frequency shift in each order of scattering; they are separated by factors of $(1 + |\beta|)/(1 - |\beta|)$ in frequency. *Right*: Angular distribution of the unscattered photons ($\omega_{\text{out}} = \omega_{\text{in}}$) with respect to the magnetic polar axis. In both cases, the plots in the top row assume a monoenergetic particle distribution (eq. [36]) with mean drift speed $\bar{\beta} = 0.5$, total width $\Delta\beta = 0.1$, and unidirectional particle flow. The plots in the bottom row assume the same distribution function, but a bidirectional particle flow.

$\bar{\beta} = 0.5$, $\Delta\beta = 0.1$, and particle flow in either one or both directions along the magnetic field. The two curves in each graph represent the injection of the seed photons in the two polarization eigenmodes.

The output spectrum has a sharp peak at $\omega_{\text{out}} = \omega_{\text{in}}$. The fraction of the seed photons that escape unscattered is shown in Figure 13 (*right column*). It is higher for the *O*-mode than for the *E*-mode, because the *O*-mode cross section has an additional factor of $(\mu')^2$, where $\mu' = \hat{\boldsymbol{k}}' \cdot \boldsymbol{B}$ is evaluated in the rest frame of the charge (eqs. [13] and [15]). The fraction of unscattered photons is highest along the two magnetic poles, where the optical depth goes to zero. Here it is independent of the polarization of the seed photons, because the two eigenmodes are degenerate when a photon propagates nearly parallel to $\boldsymbol{B}$.

The fraction of unscattered *O*-mode photons shows a third peak, which arises because the cyclotron optical depth vanishes where $\mu = \bar{\beta}$. This condition is equivalent to $\mu' = 0$; the photon propagates orthogonally to the magnetic field in the rest frame of the charge. (It is satisfied at $\mu_k \simeq 2.77$ for radially moving photons in a dipole magnetic field, where the particle drift is in only one direction along the field at a speed $\bar{\beta} = 0.5$. The small bump in the *E*-mode curve at this angle is a numerical artifact.)

Above the input frequency, the escaping photons have an approximately power-law distribution. The power-law tail is present, because (1) the optical depth τ through the corona is independent of resonant frequency (eq. [11]), and (2) the particle distribution function is assumed to be independent of position. It follows from (1) that each photon has a probability

$$P(n) = [1 - \exp(-\tau)]^n \qquad (A1)$$

of undergoing n scatterings. At the same time, (2) implies that the frequency increment $\Delta\omega$ due to backscattering is independent of the scattering order. The probability that a photon is upscattered from a frequency ω_{in} to $\omega_n = (1 + \Delta\omega/\omega)^n \omega_{\text{in}}$ is therefore

$$P(\omega_n) = \left(\frac{\omega_n}{\omega_{\text{in}}}\right)^{\{\ln[1-\exp(-\tau)]/\ln[1+\Delta\omega/\omega]\}}. \qquad (A2)$$
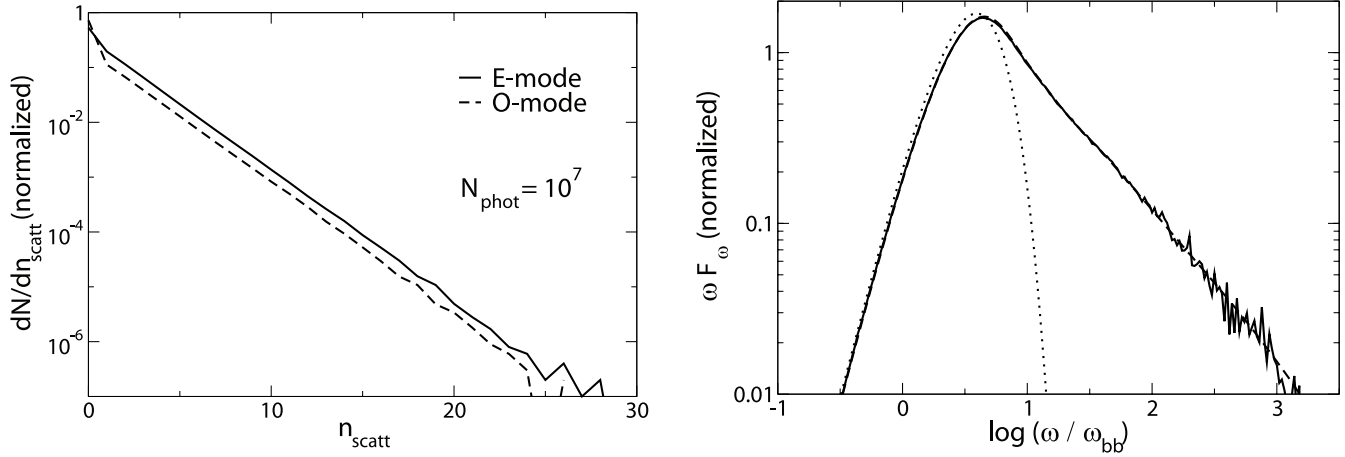
FIG. 14.—*Left*: Distribution of number of scatterings for the simulation shown in Fig. 13 (*top row*). As expected in a multiple scattering process with optical depth independent of the order of scattering (eq. [A2]), the distribution is exponential. Both seed polarizations generate the same slope, although the number of unscattered photons is bigger for the *O*-mode due to its smaller mean optical depth. *Right*: Energy spectrum for the same simulation parameters and *E*-mode seed photons, but with a different handling of the input frequency distribution. The solid curve shows the result obtained by drawing frequencies directly from a blackbody distribution (eq. [46]), whereas the dashed curve is obtained by convolving the response function of a monochromatic seed spectrum (frequency $2.82 k_B T_{bb}/\hbar$; Fig. 13, *left column*) with a blackbody distribution. Energy spectra are normalized so that the area of the Planck function is unity.

The power-law index is negative here because $\Delta\omega > 0$. It is of order unity when the particle drift is mildly relativistic, because $\Delta\omega/\omega \sim 1$. A more precise analytic calculation of the spectral slope is very difficult in practice, because τ and $\Delta\omega/\omega$ depend on μ and β in a nonlinear manner. See Pozdnyakov et al. (1983) for a general review of the effects of multiple nonresonant Compton scattering in X-ray spectra.

The spectral signature of the first few orders of scattering is apparent in Figure 13. The maximum frequency following the first backscattering is given by $\omega_{out}/\omega_{in} = (1 + |\bar{\beta}|)/(1 - |\bar{\beta}|)$, and following the second by $[(1 + |\bar{\beta}|)/(1 - |\bar{\beta}|)]^2$. One also sees the effect of downscattering to a frequency $[(1 - |\bar{\beta}|)/(1 + |\bar{\beta}|)]\omega_{in}$, since some of the charges are flowing outward (in at least one hemisphere). The low-frequency spectral slope is generally harder than the Rayleigh-Jeans value of 2, which means that the output spectrum has a nearly Rayleigh-Jeans shape at low frequencies when the input spectrum is a single-temperature blackbody. The observation of a flatter spectrum at lower frequencies in some AXP sources (Durant & van Kerkwijk 2006b) therefore points to the presence of temperature gradients across the neutron star surface.

The distribution of number of scatterings n is shown in Figure 14 (*left*) for the case of unidirectional particle flow (and the same simulation parameters as in Fig. 13). Matching the power-law slope with equation (A1), one infers a small average optical depth per scattering, $\tau \simeq 0.02$, for $\Delta\phi_{N-S} = 1$ and $\bar{\beta} = 0.5$. Both seed photon polarizations produce nearly the same slope. The simulation includes enough photons ($N = 10^7$) to obtain good statistics for the first $\sim$20–25 scatterings.

The output energy spectrum resulting from the input of a single-temperature blackbody is plotted in Figure 14 (*right*). Here two methods are used, which give nearly identical results. The solid curve shows the result obtained by drawing the seed photon frequencies directly from a blackbody number distribution (eq. [46]); the dashed curve shows the result obtained by using a single input frequency (ω_{peak}, eq. [49]) and then convolving the output spectrum with a blackbody. The main advantage of the second method is that the output spectrum is somewhat smoother, and we adopt it throughout this paper.

The energy spectra obtained with the current code were cross-checked with the output from a Monte Carlo code written previously by one of the authors (C. T.), which assumed a (split) monopole magnetic field geometry and a monoenergetic particle spectrum and calculated the position of successive scattering surfaces by a different (geometric) method. This previous code treated the transport of a photon within a resonant surface in a one-dimensional approximation. The two codes gave identical results for the high-energy power-law index, given the same field geometry, angular distribution of optical depth ($\sin^2\theta$; eq. [11]), and particle drift speed. The output spectrum differed only in some details in the shape of the peaks at the first and second scattering orders, which were ascribable to the neglect of the spatial curvature of the resonant surface in the one-dimensional code. In particular, a photon that is scattered in a direction tangent to the resonant surface sees an unrealistically high optical depth when the surface curvature is neglected. This resulted in the presence of a spurious dip at a frequency ($\omega_{out}/\omega_{in}) = 1/(1 - |\bar{\beta}|)$ in the one-dimensional output spectrum.

A2. LINE-OF-SIGHT DEPENDENT QUANTITIES

In this paper we calculate pulse profiles in different frequency bands (eq. [61]) and along specific lines of sight. Shown in Figure 15 (*left*) is the angular distribution of emission, equation (50), for the same simulation shown in Figure 13, assuming *E*-mode seed photons. These angular distributions are asymmetric with respect to $\mu_k = 0$, which allows for large pulsed fractions. The higher photon flux in the southern magnetic hemisphere ($\mu_k < 0$) reflects the southward drift of the charges near the magnetic equator (where the optical depth is largest). The angular distribution in the two lowest frequency bands also reflects the contribution of unscattered seed photons, which peaks along the magnetic poles (see Fig. 13, *right column*). A much larger fraction of the photons in bands III and IV have undergone at least one scattering.

Because only a finite number of photons are evolved in each simulation, a pulse profile can be obtained only by averaging the photon flux over some angular cone of half-width θ_{beam} (as in eq. [52]). In reality, $\theta_{beam} \simeq R_{res}/D \simeq 10^{-15}$ for a source of size $R_{res} \sim 100$ km
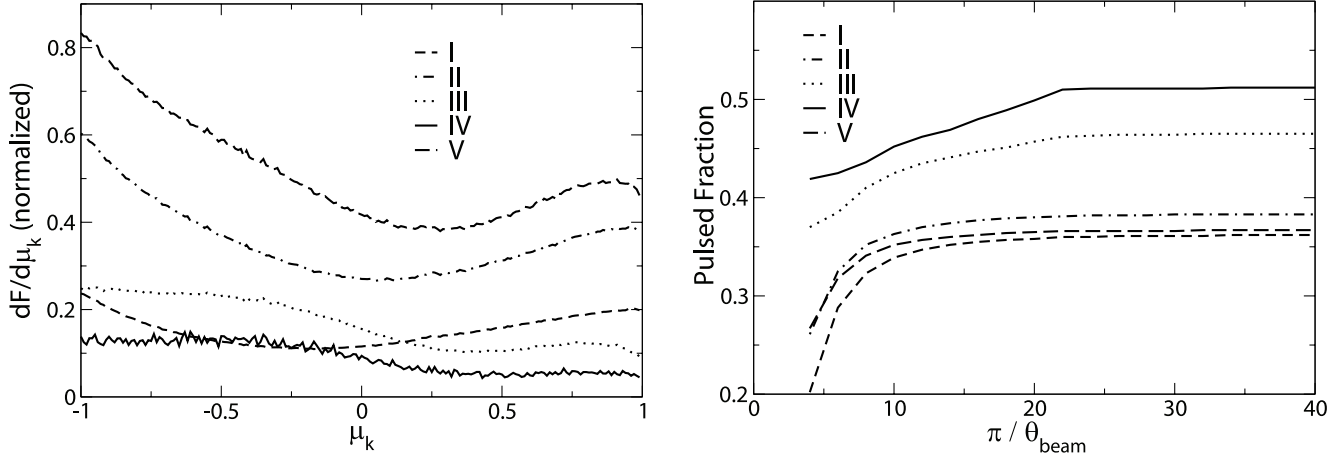
Fig. 15.—*Left*: Angular distribution of outgoing photons (eq. [50]) in the five energy bands defined in eq. (61). Bands III and IV contain most of the photons in the nonthermal tail of the spectrum, which is generated by multiple resonant scattering. *Right*: Pulsed fraction as a function of beam angle $\theta_{\rm beam}$ obtained from the angular distributions shown in the left panel. Convergence to 1% in all bands is achieved for $\theta_{\rm beam} = \pi/20 = 9°$.

(eq. [6]) at a distance $D \sim 3$ kpc. In practice, $\theta_{\rm beam}$ is taken to be the largest value for which the pulse profile has essentially converged to a constant shape and faithfully reproduces the result for $\theta_{\rm beam} \simeq 0$. As a measure of convergence, we calculated the pulsed fraction as a function of beam width for a few representative profiles and found convergence to within $\sim 1\%$ at $\theta_{\rm beam} = \pi/20 = 9°$ (see Fig. 15, *right*). In this calculation, the angular grid is taken to have a size $d\mu' \simeq d\phi' \simeq (1 - \mu_{\rm beam})/2 \simeq (\theta_{\rm beam}/2)^2$, which yields a large number of angular cells within the beam.

REFERENCES

Arras, P., Cumming, A., & Thompson, C. 2004, ApJ, 608, L49
Basko, M. M., & Sunyaev, R. A. 1975, A&A, 42, 311
Beloborodov, A. M., & Thompson, C. 2007, ApJ, 657, 967
Canuto, V., Lodenquai, J., & Ruderman, M. 1971, Phys. Rev. D, 3, 2303
Dubinski, J., Humble, R. J., Loken, C., Pen, U.-L., & Martin, P. G. 2003, in Proc. 17th Annu. Int. Symp. High Perf. Comp., ed. D. Senechal (Sherbrooke: NRC)
Durant, M., & van Kerkwijk, M. H. 2006a, ApJ, 650, 1070
———. 2006b, ApJ, 650, 1082
Esposito, P., Mereghetti, S., Tiengo, A., Sidoli, L., Feroci, M., & Woods, P. M. 2007, A&A, 461, 605
Gavriil, F. P., & Kaspi, V. M. 2004, ApJ, 609, L67
Geppert, U., Küker, M., & Page, D. 2006, A&A, 457, 937
Göhler, E., Wilms, J., & Staubert, R. 2005, A&A, 433, 1079
Götz, D., Mereghetti, S., Tiengo, A., & Esposito, P. 2006, A&A, 449, L31
Goldreich, P., & Julian, W. H. 1969, ApJ, 157, 869
Halpern, J. P., & Gotthelf, E. V. 2005, ApJ, 618, 874
Herold, H. 1979, Phys. Rev. D, 19, 2868
Heyl, J. S., & Kulkarni, S. R. 1998, ApJ, 506, L61
Ho, W. C. G., & Lai, D. 2004, ApJ, 607, 420
Ibrahim, A. I., et al. 2001, ApJ, 558, 237
Kuiper, L., Hermsen, W., den Hartog, P. R., & Collmar, W. 2006, ApJ, 645, 556
Kuiper, L., Hermsen, W., & Mendez, M. 2004, ApJ, 613, 1173
Kulsrud, R. M. 2005, Plasma Physics for Astrophysics (Princeton: Princeton Univ. Press)
Lynden-Bell, D., & Boily, C. 1994, MNRAS, 267, 146
Lyubarsky, Y., Eichler, D., & Thompson, C. 2002, ApJ, 580, L69
Lyutikov, M., & Gavriil, F. P. 2006, MNRAS, 368, 690
Marsden, D., & White, N. E. 2001, ApJ, 551, L155
Mereghetti, S., Tiengo, A., Stella, L., Israel, G. L., Rea, N., Zane, S., & Oosterbroek, T. 2004, ApJ, 608, 427
Mereghetti, S., et al. 2005, ApJ, 628, 938
Mészáros, P. 1992, High-Energy Radiation from Magnetized Neutron Stars (Chicago: Univ. Chicago Press)
Mészáros, P., & Nagel, W. 1985a, ApJ, 298, 147
———. 1985b, ApJ, 299, 138

Nagel, W. 1980, ApJ, 236, 904
Özel, F. 2002, ApJ, 575, 397
Özel, F., Psaltis, D., & Kaspi, V. M. 2001, ApJ, 563, 255
Pérez-Azorín, J. F., Miralles, J. A., & Pons, J. A. 2006, A&A, 451, 1009
Pozdnyakov, L. A., Sobol', I. M., & Syunyaev, R. A. 1983, Sov. Sci. Rev. E, 2, 189
Pravdo, S. H., & Bussard, R. W. 1981, ApJ, 246, L115
Press, W. H., Teukolsky, S. A., Vetterling, W. T., & Flannery, B. P. 1992, Numerical Recipes in FORTRAN 77 (Cambridge: Cambridge Univ. Press)
Psaltis, D., Özel, F., & DeDeo, S. 2000, ApJ, 544, 390
Rybicki, G. B., & Lightman, A. P. 1979, Radiative Processes in Astrophysics (New York: Wiley)
Silantev, N. A., & Iakovlev, D. G. 1980, Ap&SS, 71, 45
Sobol', I. M. 1994, A Primer for the Monte Carlo Method (Boca Raton: CRC)
Thompson, C., & Beloborodov, A. M. 2005, ApJ, 634, 565
Thompson, C., & Duncan, R. C. 1996, ApJ, 473, 322
Thompson, C., Lyutikov, M., & Kulkarni, S. R. 2002, ApJ, 574, 332
Tiengo, A., Mereghetti, S., Turolla, R., Zane, S., Rea, N., Stella, L., & Israel, G. L. 2005, A&A, 437, 997
Wang, J. C. L., Wasserman, I. M., & Lamb, D. Q. 1993, ApJ, 414, 815
Wang, J. C. L., Wasserman, I. M., & Salpeter, E. E. 1988, ApJS, 68, 735
Wasserman, I., & Salpeter, E. 1980, ApJ, 241, 1107
Wolfson, R. 1995, ApJ, 443, 810
Woods, P. M., Kouveliotou, C., Finger, M. H., Göğüş, E., Wilson, C. A., Patel, S. K., Hurley, K., & Swank, J. H. 2007, ApJ, 654, 470
Woods, P. M., Kouveliotou, C., Göğüş, E., Finger, M. H., Swank, J. H., Markwardt, C. B., Hurley, K., & van der Klis, M. 2002, ApJ, 576, 381
Woods, P. M., Kouveliotou, C., Göğüş, E., Finger, M. H., Swank, J. H., Smith, D. A., Hurley, K., & Thompson, C. 2001, ApJ, 552, 748
Woods, P. M., & Thompson, C. 2006, in Compact Stellar X-ray Sources, ed. W. H. G. Lewin & M. van der Klis (Cambridge: Cambridge Univ. Press), 547
Woods, P. M., et al. 2004, ApJ, 605, 378
Yahel, R. Z. 1979, ApJ, 229, L73
Zheleznyakov, V. V. 1996, Radiation in Astrophysical Plasmas (Dordrecht: Kluwer)